Inorganic Chemistry

Article

pubs.acs.org/IC

Quantifying the Electron Donor and Acceptor Abilities of the Ketimide Ligands in M(N=C^{t}Bu$_2$)$_4$ (M = V, Nb, Ta)

Peter L. Damon,[†] Cameron J. Liss,[‡] Richard A. Lewis,[†] Simona Morochnik,[†] David E. Szpunar,[‡] Joshua Telser,*[,‡] and Trevor W. Hayton*[,†]

[†]Department of Chemistry and Biochemistry, University of California, Santa Barbara, California 93106, United States

[‡]Department of Biological, Chemical and Physical Sciences, Roosevelt University, 430 South Michigan Avenue, Chicago, Illinois 60605-1394, United States

Supporting Information

ABSTRACT: Addition of 4 equiv of Li(N=C^{t}Bu$_2$) to VCl_3 in THF, followed by addition of 0.5 equiv of I_2, generates the homoleptic V(IV) ketimide complex, V(N=C^{t}Bu$_2$)$_4$ (**1**), in 42% yield. Similarly, reaction of 4 equiv of Li(N=C^{t}Bu$_2$) with $NbCl_4(THF)_2$ in THF affords the homoleptic Nb(IV) ketimide complex, Nb(N=C^{t}Bu$_2$)$_4$ (**2**), in 55% yield. Seeking to extend the series to the tantalum congener, a new Ta(IV) starting material, $TaCl_4$(TMEDA) (**3**), was prepared via reduction of $TaCl_5$ with Et_3SiH, followed by addition of TMEDA. Reaction of **3** with 4 equiv of Li(N=C^{t}Bu$_2$) in THF results in the isolation of a Ta(V) ketimide complex, Ta(Cl)(N=C^{t}Bu$_2$)$_4$ (**5**), which can be isolated in 32% yield. Reaction of **5** with Tl(OTf) yields Ta(OTf)(N=C^{t}Bu$_2$)$_4$ (**6**) in 44% yield. Subsequent reduction of **6** with Cp*$_2$Co in toluene generates the homoleptic Ta(IV) congener Ta(N=C^{t}Bu$_2$)$_4$ (**7**), although the yields are poor. All three homoleptic group 5 ketimide complexes exhibit squashed tetrahedral geometries in the solid state, as determined by X-ray crystallography. This geometry leads to a $d_{x^2-y^2}^1$ ($^2B_1$ in D_{2d}) ground state, as supported by DFT calculations. EPR spectroscopic analysis of **1** and **2**, performed at X- and Q-band frequencies (~9 and 35 GHz, respectively), further supports the $^2B_1$ ground-state assignment, whereas comparison of **1**, **2**, and **7** with related group 5 tetra(aryl), tetra(amido), and tetra(alkoxo) complexes shows a higher M−L covalency in the ketimide−metal interaction. In addition, a ligand field analysis of **1** and **2** demonstrates that the ketimide ligand is both a strong π-donor and strong π-acceptor, an unusual combination found in very few organometallic ligands.

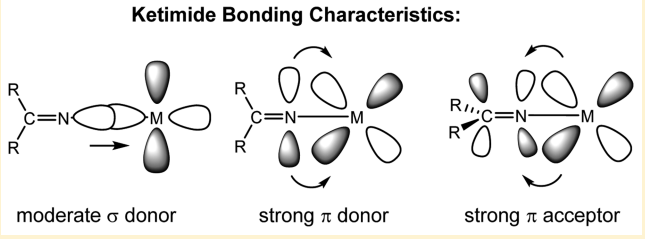

INTRODUCTION

The ketimide ligand, $[N{=}CR_2]^-$, has proven to be adept at stabilizing high oxidation states, both for transition metal ions and also the actinides.[1−7] For example, in 2010, we reported the synthesis of an isolable Fe(IV) ketimide complex, Fe(N=C^{t}Bu$_2$)$_4$,[3] a rare example of an MX_4-type complex of the late first-row transition metals.[8] Our group also synthesized the homoleptic Mn(IV) and Co(IV) ketimides, M(N=C^{t}Bu$_2$)$_4$ (M = Mn, Co),[4,6] whereas Hoffman and co-workers reported the isolation of Cr(N=C^{t}Bu$_2$)$_4$.[9] In addition, Kiplinger and co-workers reported the formation of a rare U(V) organometallic, Cp*$_2$U(NDipp)(N=CPh$_2$) (Dipp = 2,6-^{i}Pr$_2$C$_6$H$_3$), stabilized by inclusion of the ketimide ligand.[2] The ability of the ketimide ligand to stabilize high oxidation states likely stems from the orbitals available for the metal−ketimide interaction. DFT calculations on Cr(N=C^{t}Bu$_2$)$_4$ and Co(N=C^{t}Bu$_2$)$_4$ reveal that the ketimide ligand is a strong σ- and π-donor and, as such, should be adept at satisfying the 4+ charge of an M(IV) ion. Interestingly, however, the ketimide ligand also appears to be a good π-acceptor, at least according to DFT calculations.[6,7,9] The unusual combination of π-donor and π-acceptor abilities is made possible by the presence of a π-donating nitrogen lone pair and a π-accepting C=N antibonding orbital, which is orthogonal to the aforementioned nitrogen lone pair. Moreover, an energy decomposition analysis calculation on Co(N=C^{t}Bu$_2$)$_4$ suggests that the Co−N π-back-donation interaction accounts for a sizable (ca. 25%) portion of the total Co−N bonding energy in this complex.[6] This finding was somewhat unanticipated, yet it is significant because it suggests that the combined donor/acceptor properties of the ketimide ligand could engender unique structure and reactivity.

To better understand the electronic properties of the ketimide ligand, we endeavored to synthesize the tetrakis(ketimide) group 5 complexes, M(N=C^{t}Bu$_2$)$_4$ (M = V, Nb, Ta), as the d^1 electronic configuration within these complexes would render them amenable to characterization by a wide variety of spectroscopic techniques, including UV−vis and EPR spectroscopies, which could shed further light on the π-bonding and π-accepting properties of this class of ligand. Herein, we describe the synthesis and comprehensive spectroscopic characterization of M(N=C^{t}Bu$_2$)$_4$ (M = V, Nb, Ta). Most significantly, this study provides experimental confirmation that the ketimide ligand is, in fact, a good π-acceptor, knowledge

Received: September 2, 2015
Published: September 30, 2015

DOI: 10.1021/acs.inorgchem.5b02017
Inorg. Chem. 2015, 54, 10081−10095

Scheme 1

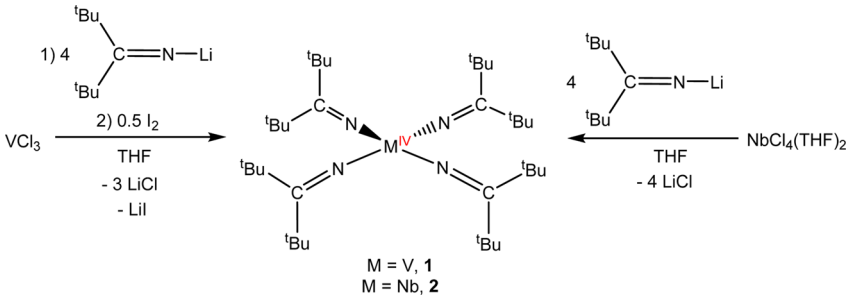

Scheme 2

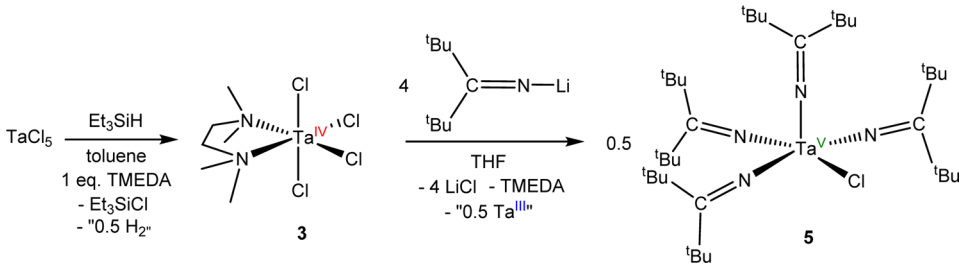

that is essential for the further development of the ketimide moiety for use as a coligand in metal-centered catalysis. In addition, we describe the synthesis of $TaCl_4$(TMEDA), a potentially useful synthon for Ta(IV) chemistry.

RESULTS AND DISCUSSION

Synthesis. Addition of 4 equiv of Li(N=C^{t}Bu$_2$) to VCl_3, in THF, affords a deep green solution. Subsequent addition of 0.5 equiv of I_2 to this solution yields the homoleptic V(IV) ketimide complex, V(NC^{t}Bu$_2$)$_4$ (**1**), in moderate yields, after workup (Scheme 1). Its niobium congener is accessible via a similar metathetical protocol. Thus, addition of 4 equiv of Li(N=C^{t}Bu$_2$) to $NbCl_4(THF)_2$,[10] in THF, affords a dark brown solution, which, after workup, yields the analogous homoleptic Nb(IV) ketimide complex, Nb(NC^{t}Bu$_2$)$_4$ (**2**), in moderate yields (Scheme 1). As a solid, complex **1** is dark orange-brown; however, it is dark green in solution. Complex **2** is dark brown, both in the solid state and in solution. Both complexes are very soluble in nonpolar solvents, such as hexanes, toluene, and Et_2O. They are also very soluble in THF but are insoluble in acetonitrile. Complexes **1** and **2** decompose in the presence of CH_2Cl_2.

The ^{1}H NMR spectrum of **1** in C_6D_6 exhibits a broad resonance centered at 3.84 ppm (fwhm = 900 Hz), which is assignable to the *tert*-butyl protons of the ketimide ligand. Similarly, the ^{1}H NMR spectrum of **2** in C_6D_6 exhibits a broad resonance centered at 6.80 ppm (fwhm = 850 Hz), which is assignable to the *tert*-butyl protons of the coordinated ketimide ligand. Interestingly, unlike previously reported transition metal ketimide complexes from our group,[3,4,6,7] complex **1** is thermally stable: thermolysis of a C_6D_6 solution of **1** at 70 °C for 2 h does not result in any signs of decomposition (Figure S2).

We next sought to synthesize the tantalum congener to complexes **1** and **2**; however, unlike Nb, an easily prepared Ta(IV) starting material has yet to be reported. For example, $TaCl_4(THF)_2$ is unknown, and although $TaCl_4$ is known, its preparation is not straightforward.[11,12] In an effort to synthesize a convenient Ta(IV) synthon, we explored the reduction of $TaCl_5$ with a readily available silane, Et_3SiH. Reaction of $TaCl_5$ with 1 equiv of $HSiEt_3$ in toluene, followed by addition of TMEDA, affords $TaCl_4$(TMEDA) (**3**), which can be isolated as an orange crystalline solid in 87% yield after workup (Scheme 2). The synthesis of **3** mirrors that of $TaCl_3$ from $TaCl_5$ and BTCD (BTCD = 3,6-bis(trimethylsilyl)-1,4-cyclohexadiene), which also generates R_3SiCl as a byproduct.[13] Complex **3** is soluble in CH_2Cl_2, THF, and acetonitrile, but it is insoluble in hexanes and Et_2O and only sparingly soluble in toluene. Its ^{1}H NMR spectrum in CD_2Cl_2 exhibits two broad singlets, at 2.72 and 8.76 ppm, in a 3:1 ratio. These are assignable to the methyl and methylene resonances of the TMEDA moiety, respectively, and are shifted significantly from those observed for free TMEDA, consistent with coordination of TMEDA to a paramagnetic metal center. Complex **3** was also characterized by X-ray crystallography (see Supporting Information for full details). Interestingly, the reduction of $TaCl_5$ with Et_3SiH also affords a second, minor product, which can be isolated as a pale blue, CH_2Cl_2-insoluble powder in very low yield. This material was subsequently identified as [{(TMEDA)$TaCl_2$(μ-Cl)}$_2$]-[$TaCl_6$] (**4**) by X-ray crystallography (see Supporting Information for more details).

Addition of 4 equiv of Li(N=C^{t}Bu$_2$) to **3**, in THF, affords a dark yellow-brown solution. Extraction into hexanes, filtration, and crystallization affords the Ta(V) ketimide, Ta(Cl)-(NC^{t}Bu$_2$)$_4$ (**5**), as yellow blocks in 32% yield (Scheme 2). The isolation of a Ta(V) product from this reaction suggests that addition of Li(N=C^{t}Bu$_2$) to **3** results in Ta(IV) disproportionation. However, efforts to identify and isolate the Ta(III) byproduct from the reaction have proven to be unsuccessful. The ^{1}H NMR spectrum of **5** in C_6D_6 exhibits a sharp singlet at 1.36 ppm, assignable to the *tert*-butyl protons of the ketimide ligand. Only one ketimide environment is observed, suggestive of rapid exchange between equatorial and axial ketimide ligand environments about the Ta^{5+} center (see below).

DOI: 10.1021/acs.inorgchem.5b02017
Inorg. Chem. 2015, 54, 10081−10095

Curiously, a direct synthetic route to complex **5** from $TaCl_5$ has not been forthcoming. For example, reaction of $TaCl_5$ with 4 equiv of $Li(N{=}C^tBu_2)$, in THF or DME, results in the formation of complex reaction mixtures, as determined by ^1H NMR spectroscopy. Complex **5** is present in the reaction mixture; however, it is but one of many components and is present only in low yield. To rationalize these results, we note that TaX_5 (X = Cl, Br, I) readily reacts with a variety of ethereal solvents, including DME and THF, to form alkoxides.[14,15] Thus, it seems likely that the in situ formation of a tantalum alkoxide during the reaction with $Li(N{=}C^tBu_2)$ in THF inhibits the desired salt metathesis.

Complex **5** crystallizes in the monoclinic space group $P2_1/c$ with two independent molecules in the asymmetric unit. The solid-state molecular structure of one independent molecule is shown in Figure 1. This complex exhibits a distorted square pyramidal structure, as determined by continuous shape measure (CSM = 1.14) developed by Alvarez and co-workers,[16] wherein the chloride ligand and three ketimide ligands occupy the equatorial positions, and one ketimide ligand (N3) occupies the axial position. The Ta−N bond lengths in **5** range from 1.918(4) to 1.990(5) Å and are similar to those observed in other tantalum ketimides.[17,18] In addition, the average Ta−N−C angle (172.7°) is indicative of sp hybridization at nitrogen and is suggestive of significant π-donation from the ketimide to the metal, consistent with our ligand field analysis (see below).[3,4,6,19] Finally, the Ta−Cl bond lengths (2.498(1), 2.496(1) Å) are similar to those observed for other structurally characterized Ta(V) chlorides.[14,15,20−22]

Complex **5** proved to be amenable to further synthetic manipulation. For example, reaction of **5** with 1 equiv of Tl(OTf) in hexanes resulted in a color change to deep red. Filtration, followed by crystallization from concentrated hexanes, resulted in deposition of $Ta(OTf)(N{=}C^tBu_2)_4$ (**6**) as red blocks in 44% yield (Scheme 3). Complex **6** crystallizes in the $P2_1/c$ space group, and, as observed for **5**, it exhibits a distorted square pyramidal geometry about the metal center (Figure 1). Not surprisingly, the metrical parameters of **6** are very similar to those of **5**.

With complexes **5** and **6** in hand, we probed their utility as precursors to the Ta(IV) ketimide complex, $Ta(NC^tBu_2)_4$ (**7**). However, neither **5** nor **6** proved to be very amenable to chemical reduction. For example, reduction of either **5** or **6** with KC_8 results in the observation of a mixture of products, whereas reductions with sodium metal or Na/Hg amalgam did not go to completion, even over long reaction times. In contrast, the reaction of **6** with Cp^*_2Co (Cp^* = pentamethylcyclopentadienide) appeared to be much more promising. Thus, addition of 1 equiv of Cp^*_2Co to a toluene-d_8 solution of **6** results in the formation of a broad singlet at 7.42 ppm (fwhm = 860 Hz) in the ^1H NMR spectrum, assignable to the *tert*-butyl protons of $Ta(NC^tBu_2)_4$ (**7**) (Scheme 3). Also present in the sample are resonances assignable to $[Cp^*_2Co][OTf]$. Unfortunately, most attempts to isolate complex **7** proved to be unsuccessful, in part because **7** appears to be quite temperature-sensitive. However, in a few instances, a few crystals of **7** were isolable, which permitted its characterization by X-ray crystallography (see below).

X-ray Crystallographic Analysis of $M(NC^tBu_2)_4$ (M = V, Nb, Ta). Complexes **1**, **2**, and **7** were characterized by X-ray crystallography, and their solid-state molecular structures are shown in Figure 2. A selection of relevant metrical parameters can be found in Table 1. In the solid state, **1** crystallizes in orthorhombic space group *Pnna* and exhibits a squashed tetrahedral geometry about the vanadium center, as evidenced by the two largest N−V−N bond angles (N1−V1−N1* = 133.1(1)° and N2−V1−N2* = 132.9(1)°). This corresponds to a τ_4 value of 0.67, where a τ_4 value of 1 indicates an idealized tetrahedron and a τ_4 value of 0 indicates an idealized square

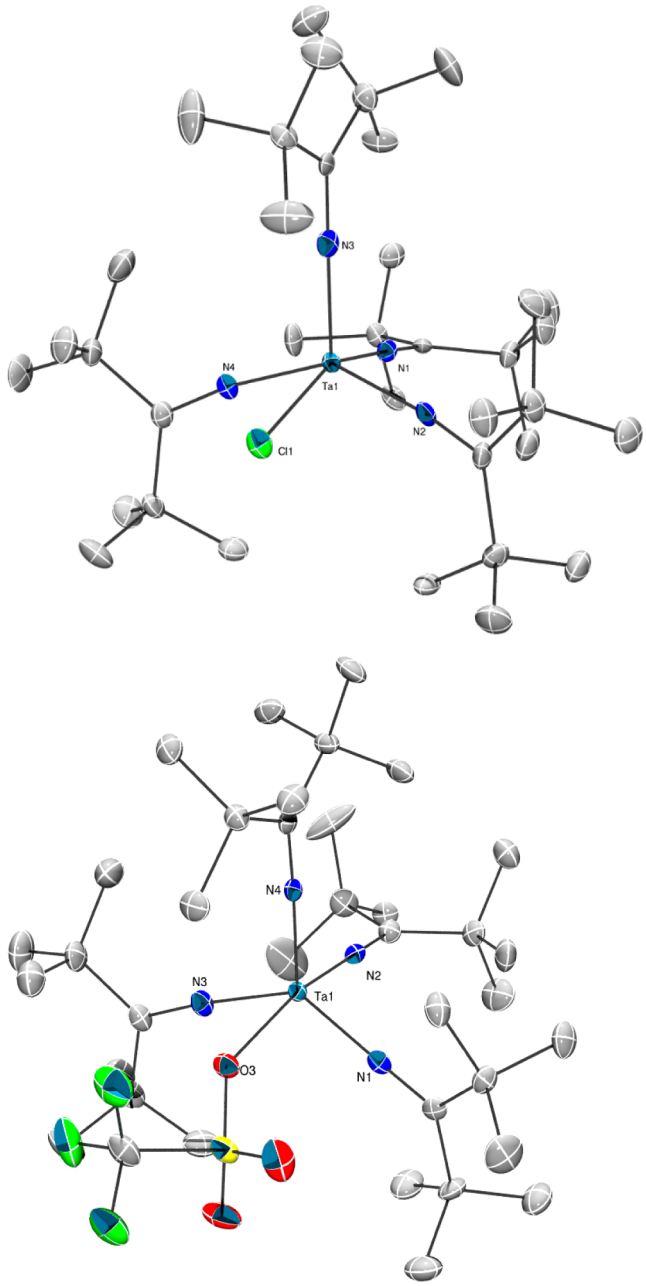

Figure 1. Solid-state molecular structures of $Ta(Cl)(NC^tBu_2)_4$ (**5**) (left) and $Ta(OTf)(NC^tBu_2)_4$ (**6**) (right) with 50% probability ellipsoids. Hydrogen atoms and a second molecule of **5** in the asymmetric unit cell are omitted for clarity. Selected bond distances (Å) and angles (deg) for **5**: Ta1−N1 = 1.958(4), Ta1−N2 = 1.967(4), Ta1−N3 = 1.922(4), Ta1−N4 = 1.982(4), Ta1−Cl1 = 2.498(1), N2−Ta1−Cl1 = 79.0(1), N4−Ta1−Cl1 = 79.1(1), N1−Ta1−Cl1 = 156.4(1), N3−Ta1−Cl1 = 103.6(1). Selected bond distances (Å) and angles (deg) for **6**: Ta1−N4 = 1.921(2), Ta1−N2 = 1.931(2), Ta1−N1 = 1.955(2), Ta1−N3 = 1.959(3), Ta1−O3 = 2.218(2), N4−Ta1−O3 = 95.27(9), N3−Ta1−O3 = 79.99(9), N1−Ta1−O3 = 80.76(8), N2−Ta1−O3 = 166.11(9).

DOI: 10.1021/acs.inorgchem.5b02017
Inorg. Chem. 2015, 54, 10081−10095

Scheme 3

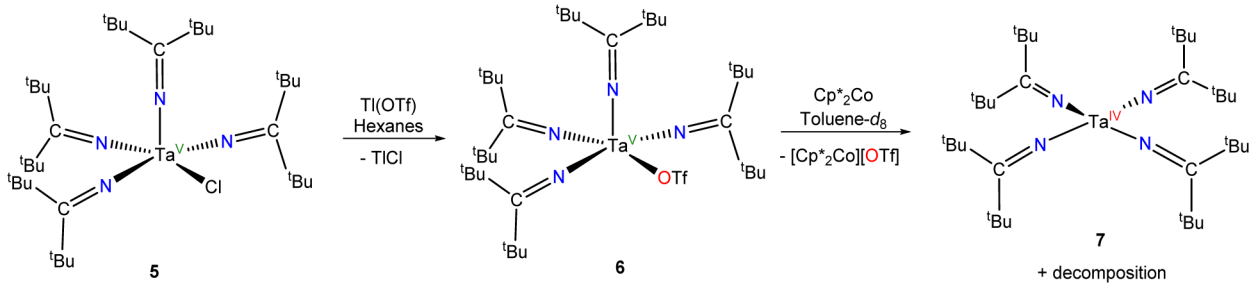

plane.[23] Complex **1** features V−N bond lengths of 1.837(1) and 1.834(1) Å. For comparison, these values are slightly shorter than those of the homoleptic V(IV) amide, $V(NMe_2)_4$, which displays V−N bond lengths of 1.866(1)−1.871(1) Å;[24] however, they are within the range exhibited by other V(V) ketimides (1.787−1.847 Å).[25−29] For further comparison, the average V−C bond length in $V(Mes)_4$ (Mes = 2,4,6-$Me_3C_6H_2$) is substantially longer (2.08 Å).[30] Finally, the V−N−C angles (V1−N1−C1= 177.2(1)° and V1−N2−C10 = 176.7(1)°) are suggestive of π-donation to the vanadium center from the ketimide ligand.

Complexes **2** and **7** feature similar squashed tetrahedral geometries in the solid state as that observed for **1**. For example, the largest N−M−N bond angles [**2**: N1−Nb1−N1* = 129.39(9)° and N2−Nb1−N2* = 129.81(9)°; **7**: N1−Ta1−N1* = 128.2(1)° and N2−Ta1−N2* = 128.5(1)°] for **2** and **7** correspond to τ_4 values of 0.72 and 0.73, respectively.[23] As anticipated, the Nb−N bond lengths in **2** (Nb1−N1 = 1.937(2), Nb1−N2 = 1.939(2) Å) are longer than those observed in **1**, consistent with the presence of the larger Nb^{4+} ion, but are shorter than those found in $Nb(NPh_2)_4$ (1.985(3)−2.029(3) Å).[31] The Ta−N bond lengths in **7** (Ta1−N1 = 1.934(2), Ta1−N2 = 1.931(2) Å) are identical to those exhibited by **2** and also similar to those exhibited by complex **5**, despite the difference in oxidation states between the two complexes. For further comparison, these values are comparable to those exhibited by $MCl(tmkh)(tBu_2pz)_2$ (M = Nb, Ta; $tmkh^{3-}$ = 2,2,6,6-tetramethyl-5-ketimidohept-3-en-3-imide; tBu_2pz^- = 3,5-di-*tert*-butylpyrazolate),[32] but they are longer than that in Cp*Ta(η^4-C_4H_6)(κ^2-*C*,*N*-C_6H_4-2-C(Me)-N).[33] Finally, the M−N−C angles in **2** (Nb1−N1−C4 = 176.5(2) and Nb1−N2−C1 = 176.5(2)°) and **7** (Ta1−N1−C1 = 176.3(2) and Ta1−N2−C10 = 174.1(2)°) are indicative of a substantial π-donation from the ketimide to the metal center.

Complex **1** is the sixth first-row transition metal $M(N{=}CtBu_2)_4$-type complex to be structurally characterized (Table 1; the present study provides the complete group 5 series; Hoffman and co-workers have previously reported the complete Group 6 series,[9] these being the only other second- and third-row $M(N{=}CtBu_2)_4$ complexes). This series of complexes exhibits an interesting correlation between the coordination geometry about the metal center and the d electron count. Specifically, we observe a gradual planarization of the geometry about the metal ion (as indicated by the τ_4 value) as the electronic configuration changes from d^0 (Ti) to d^4 (Fe). Previously, we argued that this trend was a consequence of increased crystal field stabilization that would be achieved by flattening to a D_{2d} structure.[34] Interestingly, the trend reverses at Co (τ_4 = 0.59), which features a d^5 electronic configuration. Presumably, once a d^5 configuration is achieved, at least one d electron must occupy an antibonding or partially antibonding orbital, which results in a decrease of the crystal field stabilization. This assessment was confirmed by DFT calculations on $Co(N{=}CtBu_2)_4$, which was found to have a $d_{x^2-y^2}{}^2(d_{xz,yz})^2d_{z^2}{}^1$ ($^4A_2$ in D_{2d}) ground-state electronic configuration. These calculations demonstrated that the partially occupied orbitals (d_{xz},d_{yz},d_{z^2}) all possess considerable π* Co−N character.[6] Several group 5 tetra(amido) complexes (e.g., $M(NR_2)_4$) have also been structurally characterized, and a comparison of their metrical parameters with those of **1**, **2**, and **7** is similarly informative. Most interestingly, this class of materials does not exhibit the squashed tetrahedral geometry observed in $M(N{=}CtBu_2)_4$ and, instead, exhibits only slightly distorted tetrahedral geometries. For example, the two largest N−V−N interligand angles in $V(NMe_2)_4$ are 115.28(6) and 111.42(6)°, substantial smaller than those exhibited by **1** and close to the 109.5° expected for a perfect tetrahedron.[24] Similarly, $Ta(NPh_2)_2(NEt_2)_2$ features a slightly distorted tetrahedral geometry,[35] whereas $Nb(NPh_2)_4$ and $Ta(NCy_2)_2(NEt_2)_2$ feature some modest flattening, but it is not of the magnitude observed by complexes **1**, **2**, and **7**. In particular, the two largest N−Nb−N interligand angles for $Nb(NPh_2)_4$ are 120.8(1) and 116.7(1)°,[31] and the two largest N−Ta−N interligand angles for $Ta(NCy_2)_2(NEt_2)_2$ are 123.9(1) and 123.6(1)°.[36] This difference in coordination geometry can be rationalized by arguing that the ketimide ligand is a stronger field ligand than the amide ligand and that the larger CFSE extant in the ketimide complex is enough to overcome the unfavorable steric repulsion engendered by flattening the geometry about the metal center.[35] However, this explanation cannot discriminate between the σ- and π-contributions to the overall ligand field, which differ significantly between amide and ketimide ligands (see below). Thus, to better understand this aspect of metal−ketimide bonding we performed a thorough spectroscopic analysis of complexes **1**, **2**, and **7**.

EPR Spectroscopy. The solution-phase X-band EPR spectrum of **1** in hexanes (2 mM) exhibits eight major features, consistent with a single unpaired electron coupling to the ^{51}V nucleus ($I = {}^7/_2$, ~ 100%) with $a(^{51}V)$ = 124 MHz (Figure 3). The large $a(^{51}V)$ value, along with the g value (g_{iso} = 1.988 < g_e), are consistent with a predominantly metal-centered radical. In addition, hyperfine coupling to the four ^{14}N nuclei (I = 1, 100%) of the ketimide ligand is also partly resolved ($a(^{14}N)$ = 10.5 MHz). The line widths show a strong dependence on $|m_I|$, as has been described in detail for $[VO(acac)_2]$[37] and was also seen in several V(IV) phosphine complexes.[38] For comparison with other organovanadium(IV) complexes, $Cp_2V(SPh)_2$ and $Cp_2V(S_5)$ exhibit nearly identical isotropic g and $a(^{51}V)$ values as those exhibited by complex **1**.[39,40] Also relevant are the

DOI: 10.1021/acs.inorgchem.5b02017
Inorg. Chem. 2015, 54, 10081−10095

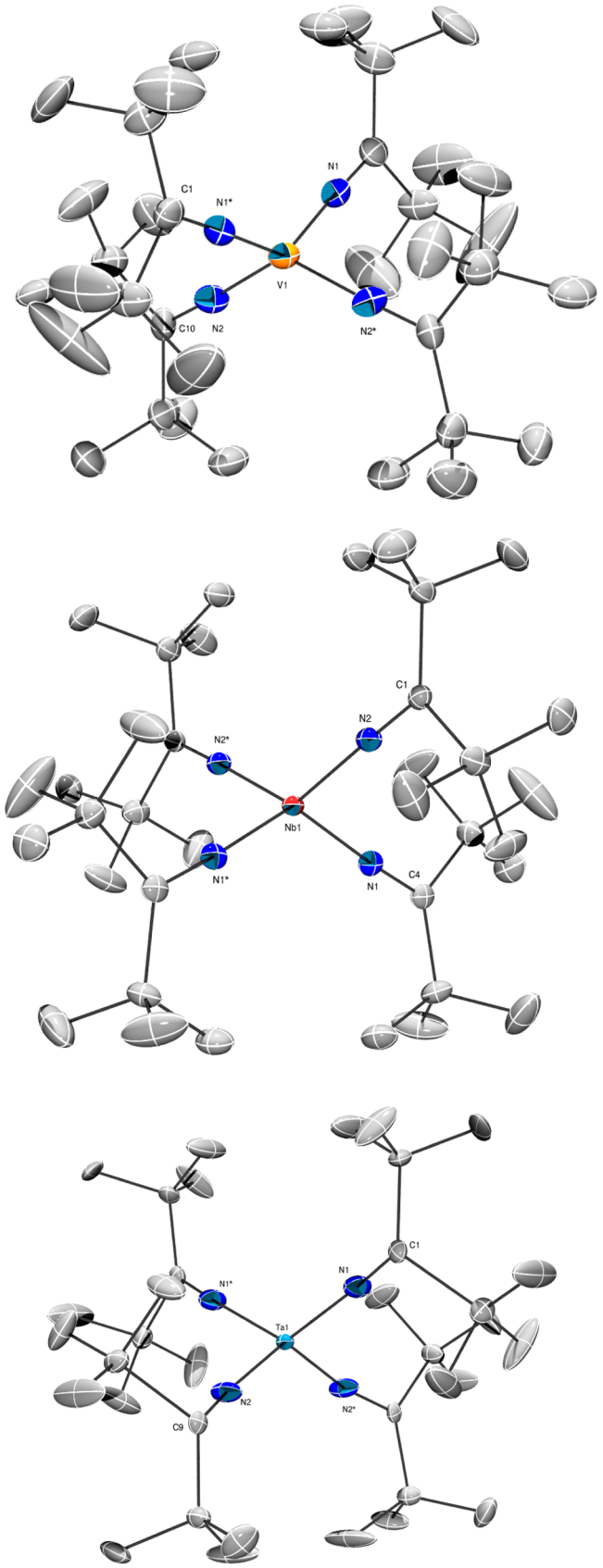

Figure 2. Solid-state molecular structures of $V(NC^tBu_2)_4$ (**1**), $Nb(NC^tBu_2)_4$ (**2**), and $Ta(NC^tBu_2)_4$ (**7**) with 50% probability ellipsoids. Hydrogen atoms are omitted for clarity. Atoms with an asterisk are generated by symmetry.

Table 1. Comparison of the Metrical Parameters for $M(N{\equiv}C^tBu_2)_4$ (M = Ti, V, Nb, Ta, Cr, Mn, Fe, Co)

M	d count	M–N distances (Å)	M–N–C angles (deg)	N–M–N angles (deg)[a]	τ_4[b]	ref.
Ti	d^0	av. 1.87	av. 175	114.9	0.96	19
				111.3		
V (**1**)	d^1	1.834(1)	176.7(1)	132.94(9)	0.67	this work
		1.837(1)	177.2(1)	133.12(9)		
Nb (**2**)	d^1	1.937(2)	176.5(2)	129.39(9)	0.72	this work
		1.939(2)	176.5(2)	129.81(9)		
Ta (**7**)	d^1	1.931(2)	176.3(2)	128.5(1)	0.73	this work
		1.934(2)	174.1(2)	128.2(1)		
Cr	d^2	1.784(2)	178.4(2)	136.1(1)	0.62	9
		1.785(2)	179.1(2)	136.2(1)		
Mn	d^3	av. 1.79	av. 176	151.1(1)	0.42	4
				150.3(1)		
Fe	d^4	1.771(3)	165.5(3)	167.1(2)	0.18	3
		1.775(3)	166.6(3)	167.6(2)		
Co	d^5	av. 1.80	av. 167	137.6(2)	0.59	6
				139.3(2)		

[a]Defined as the two largest N–M–N angles observed in the complex. [b]As defined in ref 23.

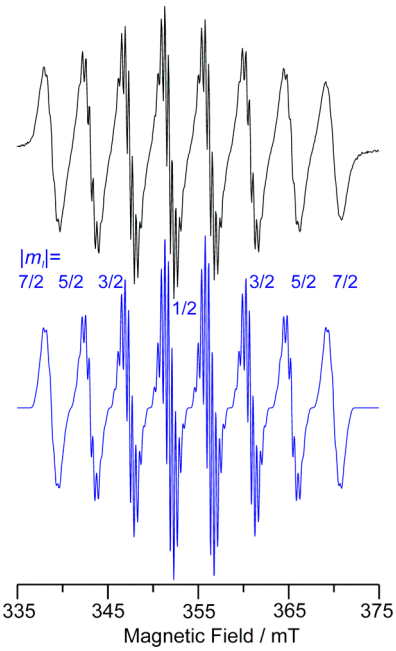

Figure 3. Room-temperature X-band EPR spectrum of **1** (2 mM in hexanes). Simulated spectrum shown in blue. Experimental conditions: microwave frequency = 9.856 GHz, microwave power = 1.0 mW, field modulation = 1.0 G, time constant = 0.32 ms, average of three 250 s scans. Simulation parameters: g = 1.9885, $a(^{51}V)$ = 124 MHz, $a(^{14}N)_4$ = 10.5 MHz, Gaussian line width = 5 MHz, to match the resolved splitting in the center of the spectrum (an expansion of this central region is shown in Figure S20, Supporting Information). The increased line broadening that occurs with higher magnitude ^{51}V m_I transitions (e.g., $\langle m_S, m_I| = \langle -1/2, \pm 7/2| \rightarrow \langle +1/2, \pm 7/2|$; see $|m_I|$ labels on simulated trace; absolute values are given because the sign of a_{iso} is unknown from experiment) is reproduced using the model of Froncisz and Hyde,[45] with their A-strain factor, c_1 (here, isotropic) = 1.5 MHz. When the ligand hyperfine coupling was not resolved, it was possible to match all transitions even more exactly (see Figure S19, Supporting Information).

DOI: 10.1021/acs.inorgchem.5b02017
Inorg. Chem. 2015, 54, 10081–10095

Table 2. Spin Hamiltonian Parameters for Group 5 Complexes Relevant to This Study

complex	g_{iso} (fluid solution)	g_{avg} (frozen solution)	$g_{\|}$, $g_{\perp}$ (frozen solution)	a_{iso} (fluid solution, MHz)	A_{avg} (frozen solution, MHz)	$A_{\|}$, $A_{\perp}$ (frozen solution, MHz)	ref.
$[V(N{=}C^tBu_2)_4]$, **1**[a]	1.9885(5)	1.983	1.979(1), 1.985(5)	124(2)	125	245(5), 65(15)	this work
$[Nb(N{=}C^tBu_2)_4]$, **2**	1.9840(5)	1.988	1.966 (2), 1.999(5)[b]	185(5)	150	300(10), 80(20)[b]	this work
$[Ta(N{=}C^tBu_2)_4]$, **7**	1.955(5)	1.979	1.998, 1.970[c]	250(10)	250	335, 210	this work
$[V(C_6Cl_5)_4]$	1.965		1.925, [1.985][d]	185		385, [85][e]	41
$[Nb(C_6Cl_5)_4]$		1.940	1.883, 1.969		371	598, 258	46
$V(Mes)_4$[f]	1.972	1.968	1.925, 1.989	172.4	189.8	370.5, 99.5	42
$V(N(C_6H_4\text{-}2\text{-}^tBu))(NHMe_2)_2Cl_2$[g]	1.973	1.973	1.948, 1.986	260	260	458, 158	47
$V(NEt_2)_4$	1.976	1.976	1.957, 1.985	180	180	372, 84	43
$V(O^tBu)_4$	1.964(5)	1.969(5)	1.940(5), 1.984(5)	192(6)	197(15)	375(15), 108(12)	44
$Cp_2V(SPh)_2$	2.00			175			40
$VCl_4(PEt_3)_2$	1.981		1.972, 1.985	252		450, 147	38
$NbCl_4(PEt_3)_2$	1.927		1.959, 1.912	381		599, 276	38
$TaCl_4(PEt_3)_2$	1.740		1.831, 1.695	514		730, 413	38
$[(MeCp)Nb(C_7H_7)]$[h]	1.986			94.5			48
$[CpTa(C_7H_7)]$[h]	1.944	1.944	1.989, 1.921	171	157	428, 22	49
$[(MeCp)Ta(C_7H_7)]$[h]	1.945	1.943	1.987, 1.921	199	192	465, 56	49
$[Cp^*Ta(C_7H_7)]$[h]	1.949	1.948	1.989, 1.927	316	306	582, 168	49
$[^{X,R}[NNN^{sq\bullet}]TaCl_3]^{-}$[i]	1.958−1.964			81−92			50, 51

[a]These parameters are based on X-band spectra. Frozen-solution Q-band spectra gave $g_{\|} = 1.979$, $g_{\perp} = 1.987$, $A_{\|}(^{51}V) = 250$ MHz, and $A_{\perp}(^{51}V) = 65$ MHz. [b]These parameters are for the majority species. The frozen-solution spectrum of **2** is very sensitive to freezing artifacts. Frozen-solution Q-band spectra gave $g_{\|} = 1.979$, $g_{\perp} = 1.995$, $A_{\|}(^{93}Nb) = 310$ MHz, and $A_{\perp}(^{93}Nb) = 80$ MHz. However, species with $A_{\|} = 365$ MHz were also observed at X-band under slower freezing conditions, which give $A_{avg} = 175$ MHz, a value much closer to the fluid-solution value. [c]These parameters roughly reproduce one species found in frozen solution. No error ranges are given because of the approximate nature of this simulation and the lack of corroborating 35 GHz EPR data, in contrast to **1** and **2**. [d]Not reported but calculated here using the reported g_{iso} and $g_{\|}$ values. [e]Not reported but calculated here using the reported a_{iso} and $A_{\|}$ values. [f]In addition to a fluid solution of $V(Mes)_4$ (Mes =2,4,6-$Me_3C_6H_2$), a single crystal of $Ti(Mes)_4$ doped with $V(Mes)_4$ was studied so that the full **g** and ^{51}V hyperfine coupling tensors were determined with high precision: $g_x = 1.984$, $g_y = 1.994$, and $g_z = 1.925$; $A_x = 80.6$, $A_y = 118.4$, and $A_z = 370.5$ MHz; these are converted to axial tensors for easier comparison with the other entries. [g]This is but one of a large number of five- and six-coordinate V(IV) complexes reported in this article; the one presented here is more relevant to the ketimides. It is representative of a series of five-coordinate V(IV) imido complexes, $V(=NR)(NHMe_2)_2Cl_2$ where R = five different bulky aryl or alkyl substituents. Their EPR parameters vary minimally as a function of R group as seen in Table 5 of Bigmore et al.[47] Their *A* values have been converted from G to MHz using their reported *g* values. [h]These are considered as Nb(IV) or Ta(IV) complexes by virtue of the cycloheptatrienyl ligand being counted as a trianion (10 π electrons, Hückel aromatic), along with the cyclopentadienyl monoanion. [i]The $^{X,R}[NNN^{sq\bullet}]^{2-}$ ligand is the semiquinone form of $^{X,R}[NNN^{cat}]^{3-}$, where, e.g., $^{OMe,iPr}[NNN^{cat}]^{3-}$ is the trianion of bis(2-isopropylamino-4-methoxyphenyl)amine (X = 4-OMe; F, H, Me, and ^{t}Bu; R = 2-^{i}Pr; 3,5-$C_6H_3Me_2$). These complexes are neither truly Ta(V) nor Ta(IV) as a result of the noninnocent ligand. Simulations of room-temperature spectra of four complexes were presented, but no parameters were given; the range of g_{iso} and a_{iso} values presented here are taken from legends to a composite figure in the Supporting Information of ref 50.

homoleptic V(IV) complexes that feature tetra(aryl), tetra(amido), and tetra(alkoxido) ligand sets.[41−44] One of the tetra(aryl) complexes was observed only in situ by Alonso et al.,[41] but another, $V(Mes)_4$, was studied not only in fluid solution but also as a doped single crystal (diamagnetic $Ti(Mes)_4$ host),[42] likely affording the most accurate and complete spin Hamiltonian parameters for any complex relevant to the present work. The EPR investigations and analysis of the tetra(amido)[43] and tetra(alkoxido)[44] complexes were also very thorough, with a variety of solvents and diamagnetic hosts (the Ti(IV) congeners) employed. These and other EPR parameters of interest are summarized in Table 2.

The room-temperature EPR spectrum of **2** in hexanes (2 mM) consists of a 10 line pattern, consistent with a single unpaired electron coupling to one ^{93}Nb center ($I = {}^9/_2$, 100%) with $a_{Nb} = 185$ MHz (Figure 4). Hyperfine coupling to ^{14}N was not resolved in this spectrum. Again, the *g* value falls within the range of a transition metal-centered radical ($g_{iso} = 1.984$). Most relevant is the structurally characterized (in contrast to its V congener) homoleptic tetra(aryl) Nb(IV) complex, $[Nb(C_6Cl_5)_4]$.[46] The spin Hamiltonian parameters for this complex are given in Table 2 and show that the ^{93}Nb hyperfine coupling constant in $[Nb(C_6Cl_5)_4]$ is much larger than in **2**. This difference, which is also seen for the V complexes, can be qualitatively explained by the greater covalency (via σ- and π-bonding; see below) in **2**, as opposed to the more ionic σ-only bonding in the pentachlorophenyl complex.

The solution-phase EPR spectrum of **7**, generated in situ in toluene-d_8 by reaction of **6** with 1 equiv of Cp^*_2Co, exhibits the expected eight line signal, consistent with a single unpaired electron coupling to ^{181}Ta ($I = {}^7/_2$, 100%). In the spectrum shown in Figure 5, complex **7** exhibits a hint of resolved hyperfine coupling to the ^{14}N nuclei of the ketimide ligand. As shown on an expanded field scale in Figure S20 (Supporting Information), we estimate this coupling at $a(^{14}N) \approx 30$ MHz. For comparison, the corresponding well-resolved central signals for **1** are also shown in Figure S20, demonstrating the good fit to that region ($|m_I| = {}^1/_2$), which is unaffected by hyperfine-dependent line broadening effects. The observed g_{iso} value (g_{iso}

DOI: 10.1021/acs.inorgchem.5b02017
Inorg. Chem. 2015, 54, 10081−10095

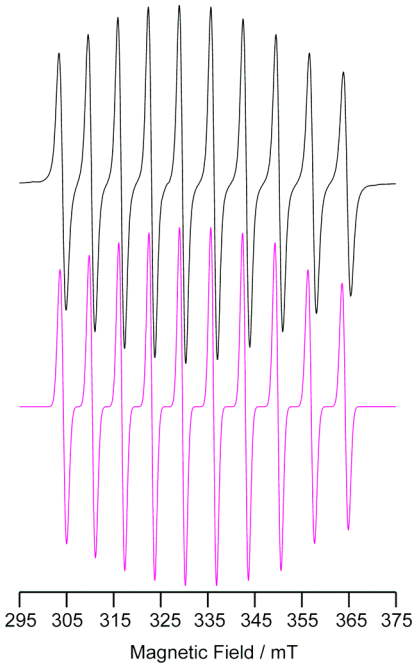

Figure 4. Room-temperature X-band EPR spectrum of **2** (2 mM in hexanes). Experimental conditions: microwave frequency = 9.290 GHz, microwave power = 1.0 mW, field modulation = 0.2 G, time constant = 20 ms, average of twenty-five 20 s scans. Simulation parameters: g = 1.9840, $a(^{93}\text{Nb})$ = 185 MHz, Gaussian line width = 20 MHz, to match the central transitions. The increased line broadening that occurs with higher magnitude ^{93}Nb m_I transitions is reproduced using the model of Froncisz and Hyde,[45] with their A-strain factor, c_1 (here, isotropic) = 2.5 MHz.

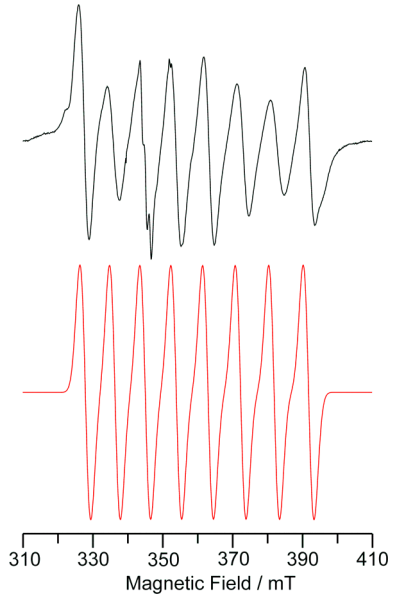

Figure 5. Room-temperature X-band EPR spectrum of **7** (0.02 mM in toluene-d_8). Experimental conditions: microwave frequency = 9.858 GHz, microwave power = 1.0 mW, field modulation = 1.0 G, time constant = 10 ms, average of twenty 10 s scans. Simulation parameters: g = 1.955, $a(^{181}\text{Ta})$ = 250 MHz, Gaussian line width = 50 MHz. No attempt was made to model any A-strain effects, in contrast to the situation for **1** (Figure 3) and **2** (Figure 4), but the ^{14}N hyperfine coupling is shown on an expanded scale in Figure S20 (Supporting Information).

= 1.955) again falls in the range of transition metal-centered radicals, and the a_{iso} value (a_{iso} = 250 MHz) continues the trend of increasing a_{iso} values of the group 5 ketimides on going down the column, despite the decrease in g_N from V to Nb to Ta. A similar trend was seen in the $MCl_4(PEt_3)_2$ (M = V, Nb, Ta) series, in which the a_{iso} values increased from 252 to 381 to 514 MHz on going down the group.[38] As seen in Table 2, the ^{181}Ta hyperfine coupling is also in the range reported for the hydrocarbyl complexes, (CpR)Ta(C_7H_7) (R = H, Me, Me_5)[49] and is much larger than that reported for a series of tantalum complexes with a noninnocent pincer ligand.[51]

Being the most stable of the three, the frozen-solution EPR spectra of **1** were investigated under a variety of experimental conditions. As shown in Figure 6, in hexanes at 125 K, complex

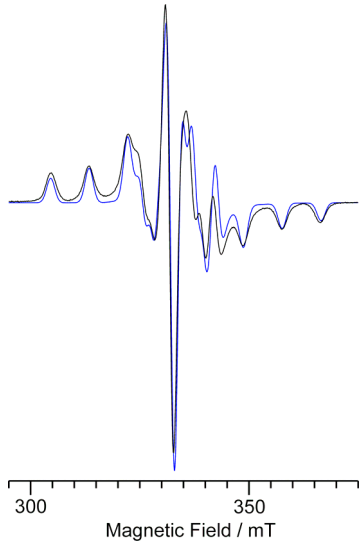

Figure 6. Frozen-solution X-band EPR spectrum (black = experimental, red = simulated) of **1** (2 mM in hexanes) at 125 K. Experimental conditions: microwave frequency = 9.296 GHz, microwave power = 2.0 mW, modulation = 0.5 G, time constant = 2.56 ms, average of thirty-three 20 s scans. Simulation parameters: **g** = [1.985, 1.985, 1.979], **A**(^{51}V) = [65, 65, 245] MHz, Gaussian line widths = 30 MHz.

1 displays average g and A values in good agreement with the room-temperature isotropic (i.e., rotationally averaged) values (see Table 2) but with significant uniaxial anisotropy, defined here as the z-direction ($A_x = A_y = A_\perp$ = 65 MHz, $A_z = A_\parallel$ = 245 MHz). Similar EPR anisotropy has been observed in the pseudo-four-coordinate V(IV) complex $[Cp_2V(dbm)][ClO_4]$ (dbm = dibenzoylmethanate)[52] and in $V(Mes)_4$.[42] Indeed, the ratio of $A_\parallel/A_\perp$ in $V(Mes)_4$ equals 3.72, and in **1**, this ratio is 3.77. The origin of this anisotropy will be discussed below. The X-band EPR spectrum of **1** recorded in toluene solution at 20 K (Figure S21, Supporting Information) was similar, but not identical, to that shown here. This may be a consequence of the tetrakis(ketimide) complexes being rather flexible, as next shown more convincingly for the Nb congener.

We also recorded the 35 GHz (Q-band) EPR spectrum of **1** at 2 K in toluene (Figure 7). Under these experimental conditions, the spectra are in rapid passage mode and appear as the absorption line shape.[53] This presentation mode is helpful for observing broad features, but it is less so for the relatively narrow lines of **1**. Nevertheless, the use of a second EPR resonant frequency is very helpful in showing the validity of a

DOI: 10.1021/acs.inorgchem.5b02017
Inorg. Chem. 2015, 54, 10081−10095

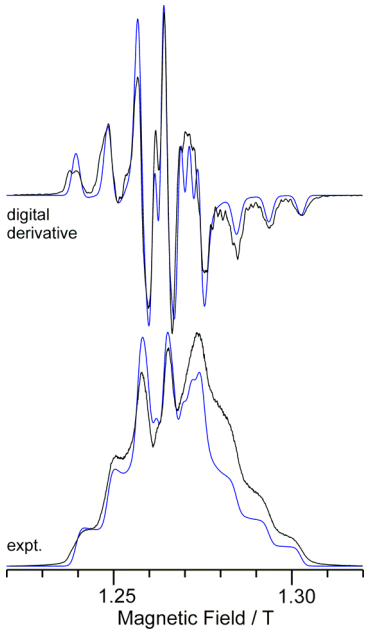

Figure 7. Low-temperature (2 K) Q-band EPR spectrum of **1** (0.1 mM in toluene). The lower pair of traces are the experimental spectrum (black trace), together with a simulation (blue trace), and the upper pair is a digital derivative with a simulation. Experimental conditions: microwave frequency = 35.2076 GHz, microwave power = 2 mW, field modulation = 1.0 G, time constant = 16 ms, single 120 s scan. Simulation parameters: **g** = [1.987, 1.987, 1.979], **A**(^{51}V) = [65, 65, 250] MHz, W = 30, 30, 35 MHz.

set of simulation parameters, as the g values are field-dependent, whereas the hyperfine couplings are not. As can be seen from the figure caption, the simulation parameters are essentially unchanged from those determined from X-band spectra (which were, in addition, recorded at higher temperature and under slow passage, i.e., normal conditions). The increase in frequency to 35 GHz, however, is not sufficient to separate the parallel from the perpendicular transitions. To achieve this, as has been shown in vanadyl complexes, microwave frequencies at 95 GHz (W-band)[54] or higher[55] would be needed.

ENDOR spectroscopy of V(IV) complexes is rather limited and has been chiefly performed on vanadyl complexes, such as in pioneering work by van Willigen and co-workers[56,57] and more recently by Britt and co-workers[58,59] and others.[60,61] We therefore recorded 35 GHz CW ENDOR spectra of complex **1**, partly to test the feasibility of ENDOR on such a system. We indeed readily observed ^{1}H, ^{14}N, and ^{51}V ENDOR from this complex, as shown in Figure S23. The ^{1}H ENDOR signals are centered at the proton Larmor frequency (~53 MHz) and show very small hyperfine coupling, as expected for the *tert*-butyl hydrogen atoms, which are relatively distant from the paramagnetic metal center. The ^{51}V ENDOR signals are of qualitative interest only, but they are consistent with $A_{\|}$ = 240 MHz (i.e., features centered at $A_{\|}/2$ = 120 MHz). The ^{14}N signals also confirm the results of EPR spectroscopy. In the absence of a complete ENDOR study, it is not appropriate to make a definitive correspondence between the ^{14}N hyperfine splitting observed by EPR and that by ^{14}N ENDOR. This is because one is comparing fluid-solution X-band EPR spectra, which provide a_{iso}(^{14}N) (i.e., an average coupling value of all molecular orientations), to frozen-solution Q-band ENDOR spectra, recorded only at $g_{\|}$, which thus provide only $A_{\|}$(^{14}N) (i.e., the coupling along the parallel (z) direction assuming colinearity of **A** and **g**). Nevertheless, $A_{\|}$(^{14}N) ≈ 14 MHz is consistent with a_{iso}(^{14}N) = 10.5 MHz and also with DFT calculations described below.

Frozen-solution EPR spectra of complex **2** proved to be more difficult to obtain as a homogeneous species, despite multiple attempts. A representative spectrum, recorded at 20 K in toluene solution, is shown in Figure 8. This spectrum clearly

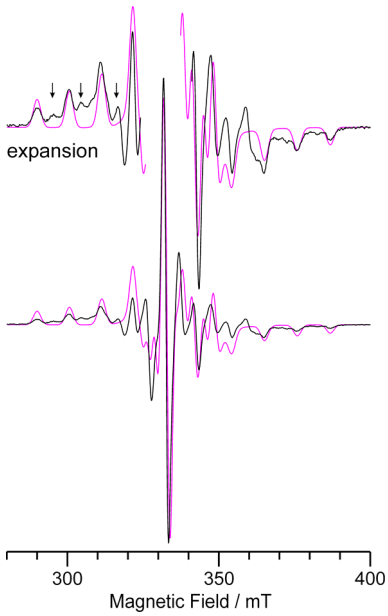

Figure 8. Frozen-solution X-band EPR spectrum of **2** (2 mM in toluene) at 20 K. Several $A_{\|}$ features of a second species are indicated by arrows in the upper, expanded vertical scale spectra; no attempt was made to simulate or quantify this minor species. Experimental conditions: microwave frequency = 9.373 GHz, microwave power = 2 mW, field modulation = 15 G, time constant = 160 ms, single 90 s scan. Simulation parameters (magenta traces): **g** = [1.999, 1.999, 1.966], **A**(^{93}Nb) = [80, 80, 300] MHz, Gaussian line widths = 35 MHz.

reveals that there are two species present in the sample, which have similar EPR signatures, suggesting that they are only slightly different structurally. Only one species is present in fluid solution (Figure 4), albeit with no resolution of ligand hyperfine, which suggests that these two species can interconvert at room temperature. We made several attempts to generate a homogeneous sample by freezing the solution as quickly as possible; however, this did not completely mitigate the heterogeneity. Nonetheless, the majority species gives average g and A values in reasonable agreement with the room-temperature isotropic values (see Table 2). The 35 GHz 2 K spectrum of **2** proved to be slightly more homogeneous (Figure 9), which may be a function of the smaller sized EPR tubes, allowing for faster freezing. The simulation parameters were essentially the same as those of the major species observed at X-band.

In keeping with the trend in stability, complex **7** gave the most problematic frozen-solution EPR behavior. There are multiple species present in these samples, albeit with similar EPR parameters. It was possible to simulate only approximately one of the species (see Figure S22, Supporting Information),

DOI: 10.1021/acs.inorgchem.5b02017
Inorg. Chem. 2015, 54, 10081−10095

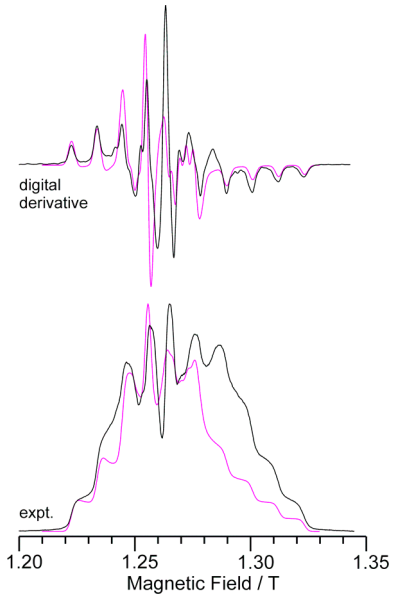

Figure 9. Low-temperature (2 K) Q-band EPR spectrum of **2** (0.1 mM in toluene). The lower pair of traces are the experimental spectrum (black trace), together with a simulation (magenta trace), and the upper pair is a digital derivative with a simulation. Experimental conditions: microwave frequency = 35.2650 GHz, microwave power = 2 mW, field modulation = 0.5 G, time constant = 16 ms, single 120 s scan. Simulation parameters: **g** = [1.995, 1.995, 1.979], **A**(^{93}Nb) = [80, 80, 310] MHz, W = 40, 40, 45 MHz.

although it gave an average ^{181}Ta hyperfine coupling consistent with the room-temperature value (see Table 2).

The results of fluid- and frozen-solution EPR studies can be combined, as was done by Alonso et al.[41] This makes use of the fact that in the frozen-solution spectra of these systems only $g_{\|}$ and $A_{\|}$ can be easily determined (single-crystal studies can provide the full tensors for both **g** and **A**, as done by Kirmse et al.),[42] but here, for **2** and especially **7**, the $g_{\perp}$ and $A_{\perp}$ values are relatively uncertain. The starting point relevant equations for an axial hyperfine interaction for a $d_{xy/x^2-y^2}{}^1$ ground state are as follows:

$$A_{\|} = -P\left[\kappa + \frac{4}{7} + \frac{3}{7}(g_e - g_{\perp}) + (g_e - g_{\|})\right],$$

$$A_{\perp} = -P\left[\kappa - \frac{2}{7} + \frac{11}{14}(g_e - g_{\perp})\right] \quad (1a,b)$$

where P is the intrinsic hyperfine coupling constant, $P = g_e g_N \beta_e \beta_N \langle r^{-3}\rangle_{av}$, which for free-ion $^{51}V^{4+}$ equals 516 MHz[62] and for free-ion $^{93}Nb^{4+}$ equals 576 MHz[62] (the value for $^{181}Ta^{4+}$ is unavailable), and κ is a unitless scaling factor to account crudely for covalency. Using the relationships

$$g_{iso} = \frac{(g_{\|} + 2g_{\perp})}{3}, \qquad a_{iso} = \frac{(A_{\|} + 2A_{\perp})}{3} \quad (2a,b)$$

By substituting eqs 1a,b into eq 2b and making use of eq 2a to substitute for $g_{\|}$ and $g_{\perp}$, one obtains

$$a_{iso} = -P[\kappa + (g_e - g_{iso})] \quad (3)$$

Subtracting eq 3 from eq 1a and substituting for $g_{\perp}$ from eq 2a gives

$$A_{\|} - a_{iso} = -P\left[\frac{4}{7} + \frac{11}{14}(g_e - g_{\|}) - \frac{5}{14}(g_e - g_{iso})\right] \quad (4)$$

allowing calculation of P in the system of interest; eq 3 then yields $|\kappa|$, since the sign of a_{iso} is not known experimentally. This method, applied to $[V(C_6Cl_5)_4]$, gave $|P|$ = 323 MHz and $|\kappa|$ = 0.54,[41] and for $[Nb(C_6Cl_5)_4]$, it gave $|P|$ = 352 MHz and $|\kappa|$ = 0.99.[46] This method had not been previously applied to $V(Mes)_4$, yet this is among the most relevant complexes to ours and that for which the best EPR data are available.[42] We thus find here for $V(Mes)_4$ that $|P|$ = 291.5 MHz and $|\kappa|$ = 0.617.[63] The tetra(amido) complex, $V(NEt_2)_4$, was reported to have $|P|$ = 330 MHz,[43] and substituting that value and their EPR data (see Table 2) into eq 3 gives $|\kappa|$ = 0.50. The tetra(alkoxido) complex, $V(O^tBu)_4$, had $|P|$ = 324 MHz, giving $|\kappa|$ = 0.55.[44] Concerning the ketimides, we calculate here for **1** that $|P|$ = 207 MHz and $|\kappa|$ = 0.59 and for **2** that $|P|$ = 194 MHz and $|\kappa|$ = 0.94.[64] If one takes the ratio of the calculated P value to the free-ion P value, then the tetra(aryl), amido, and alkoxido vanadium(IV) complexes all give values of ~0.6, whereas the V and Nb ketimides give this ratio as roughly 0.4, indicating the much higher covalency in the latter complexes.

UV−Vis Spectroscopy. Both complexes **1** and **2** exhibit rich UV−vis spectra (Figure 10). For example, the electronic

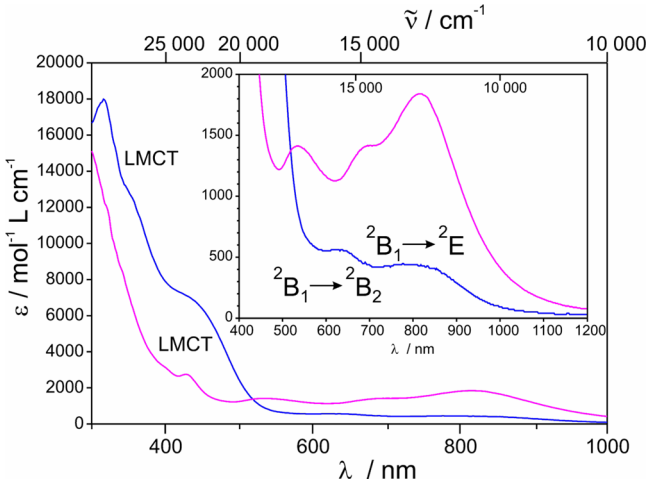

Figure 10. Room-temperature UV−vis−NIR absorption spectra of **1** (blue traces) and **2** (magenta traces) in hexanes solution. For both compounds, the bands in the approximate range 300−450 nm are due to ligand-to-metal charge transfer (LMCT) transitions. The inset shows an expansion of the vis−NIR region with d−d band assignments as described in the text.

absorption spectrum of **1** features two intense absorptions at 360 (ε = 12 000 M^{-1}·cm^{-1}) and 460 nm (ε = 6000 M^{-1}·cm^{-1}), which are both assignable to ligand-to-metal charge transfer processes, i.e., crudely represented by $[M^{IV}(^{-}N{=}C^tBu_2)] \rightarrow [M^{III}(^{\bullet}N{=}C^tBu_2)]$. Additionally, two absorptions are observed at 620 (ε = 560 M^{-1}·cm^{-1}) and 764 nm (ε = 440 M^{-1}·cm^{-1}). We have tentatively assigned these less intense bands to d−d transitions, as will be discussed in detail below. The UV−vis spectrum of **2** features an intense absorption at 320 nm (ε = 12 000 M^{-1}·cm^{-1}), which is likewise assignable to ligand-to-metal charge transfer. In addition, this spectrum features four transitions at 432 (ε = 2700 M^{-1}·cm^{-1}), 596 (ε = 1200 M^{-1}·cm^{-1}), 698 (ε = 1400 M^{-1}·cm^{-1}), and 830 nm (ε = 1800 M^{-1}·cm^{-1}), which are assignable to d−d transitions. Unfortunately,

DOI: 10.1021/acs.inorgchem.5b02017
Inorg. Chem. 2015, 54, 10081−10095

it was not possible to prepare UV−vis samples of **7** that were free of other optically absorbing components.

Ligand Field Theory Analysis. To employ a simple ligand field theory for the $[M(N{=}C^tBu_2)_4]$ complexes, we need to establish a physical model. In D_{2d} point group symmetry, the $d_{x^2-y^2}$ AO is represented by B_1, and its parentage (via ascent in symmetry) is E (together with d_{z^2}) in T_d. The d_{xy} orbital is represented by B_2, and its parentage (along with d_{xz} and d_{yz}) is T_2 in T_d. This symmetry and coordinate system are identical to that used by some of us in our previous study of $[Co(N{=}C^tBu_2)_4]$.[6] To achieve this description, we define the x and y axes as lying between the M−L bonds (bisecting the L−M−L angles) (Figure 11), which is, in any case, more appropriate for

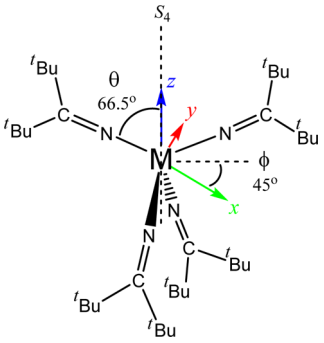

Figure 11. Structure of generic $M(N{=}C^tBu_2)_4$ complex showing coordinate system used for the AOM analysis. Two ketimide ligands are in the plane of the paper: one projects from the paper and the other is behind. The z axis (shown in blue) corresponds to the approximate S_4 axis; the x (green) and y (red) axes are rotated 45° from the ligands planes. For the AOM analysis, average θ, θ' values are used (ideal θ = 54.7356°), with an ideal S_4 axis (ϕ = 45° (as shown), 135°, 225°, 315°). For M = Ti, θ = 56.53°; for M = V (**1**), θ = 66.5° (as shown); for M = Nb (**2**), θ = 64.4°; for M = Ta (**7**), θ = 64.16°; the angle to the other pair of ligands, $\theta' \equiv 180° - \theta$.

an axial ($x = y$) system. If the x and y axes were defined along the M−L bonds, as done by Soriaga et al.,[9] then the representation of $d_{x^2-y^2}$ and d_{xy} would be reversed. Such a definition would be appropriate for C_{2v} symmetry, where x and y are symmetry inequivalent. Given the axial nature of the EPR spectra and a desire for the simplest useful model to describe $[M(N{=}C^tBu_2)_4]$ complexes, we shall use primarily D_{2d} symmetry in our simple ligand field model.

We can now begin to describe the ketimide MOs involved in bonding using the angular overlap model (AOM) with an ideal S_4 axis defining z and the x and y axes between the bonds, as described above (see Figure 11). The angle θ is given by the relevant crystal structures. This geometrical model is sufficient for the simple nature of our analysis. Soriaga et al. did not mention σ-bonding in this class of complexes,[9] but we note that the ketimide ligand is likely a strong σ-donor. This interaction alone could potentially lead to a large splitting between the $e(d_{z^2},d_{x^2-y^2})$ and $t_2(d_{xz},d_{yz},d_{xy})$ metal ion orbitals. This splitting, for a T_d ML_4 complex, is given by $\Delta_{tet} = {}^4/_3\varepsilon_\sigma$. For illustrative purposes, we begin with only σ-bonding and the structure of the Ti(IV) congener, which has θ only ∼2° away from ideal tetrahedral (τ = 0.96).[19] We can moderately well fit the two observed putative d−d electronic transitions for **1** using this nearly tetrahedral model with ε_σ = 10 610 cm^{-1}. The ground state is $^2B_1(d_{x^2-y^2}{}^1)$, with the $^2A_1(d_{z^2}{}^1)$ excited state barely higher in energy (∼100 cm^{-1}). The transition $^2B_1 \rightarrow {}^2A_1$ is forbidden in D_{2d} point group symmetry,[65] but the $^2B_1 \rightarrow {}^2E$ ($d^1_{xz,yz}$) transition is allowed with xy polarization.[66] It is calculated to occur at 13 470 cm^{-1}, reasonably close to experiment (12 800 cm^{-1}, based on the band centers on an energy scale). For comparison, VCl_4 has Δ_{tet} = 7900 cm^{-1},[67] and $V(Mes)_4$ has Δ_{tet} = 13 370 cm^{-1},[30] giving ε_σ = 10 030 cm^{-1}. The higher energy transition is $^2B_1 \rightarrow {}^2B_2$ (d^1_{xy}), which is calculated to occur at 15 410 cm^{-1}, also reasonably close to experiment (16 000 cm^{-1}). Although this transition is forbidden,[68] it may become partially allowed by vibronic coupling, and its intensity perhaps also benefits from underlying charge transfer band(s).[69] Vibronic coupling would be reasonable for **1** due to the Jahn−Teller effect. Tetrahedral nd^1 is a classic Jahn−Teller active system, being $e^1t_2^0$, the electron analogue to the hole configuration $t_2^6e^3$, as exemplified by octahedral Cu(II), for which vibronic coupling of an e_g mode (ν_2) provides a mechanism for Jahn−Teller distortion.[70] $V(Mes)_4$ and VCl_4 are complexes with, respectively, only σ-bonding and cylindrical π-bonding, which makes them better candidates for this effect than ketimides with their unsymmetrical π-bonding (i.e., making the distortion a pseudo Jahn−Teller effect). Although a (true) Jahn−Teller effect was not invoked to justify the D_{2d} symmetry of $V(Mes)_4$ (this complex may have significant steric effects),[30] VCl_4 may exhibit this effect,[67] and it may be related to the observation of a nominally forbidden band in **1**.

However, a problem arises when we use the actual geometry of **1** (Figure 11). In this case, the greater distortion from tetrahedral geometry makes it impossible to fit both electronic transitions simultaneously. Either the lower or the higher band can be fit exactly using the $^2B_1 \rightarrow {}^2E$ assignment (with ε_σ = 16 000 cm^{-1} or ε_σ = 20 000 cm^{-1}, respectively), but not both, unless the symmetry is lowered such that the four ketimide ligands are divided into two pairs: two with the lower ε_σ value and two with the higher. This C_{2v} split is large but not inconceivable.[71] The problem is not so much symmetry but that these ε_σ values are *extremely* high.[72,73] Thus, a model with only σ-bonding is unsatisfying.

Clearly, π-bonding must be considered, as was the case with the more electron-rich Co(IV) congener.[6] Soriaga et al. identified the ketimide MOs having π-interactions with an electron-poor metal ion.[9] These are shown in Figure 12, which is inspired by their work and is also a cartoon version of the more recent DFT results depicted in Figure 2 of Lewis et al.[6] The occupied, π-donor MO that interacts strongly with d_{z^2} (and not at all with $d_{x^2-y^2}$ in ideal tetrahedral geometry) is labeled π−c,[72] with interaction parametrized by $\varepsilon_{\pi-c}$, increasing the energy of d_{z^2}. The unoccupied, π-acceptor MO that interacts with $d_{x^2-y^2}$ (and not at all with d_{z^2} in ideal tetrahedral geometry) is labeled π−s, with interaction parametrized by $\varepsilon_{\pi-s}$, decreasing the energy of $d_{x^2-y^2}$. The d_{xz},d_{yz} AOs are moderately affected by these π-bonding interactions using the AOM (see Table S2, Supporting Information), but in V(IV) (and Cr(IV)), these empty AOs are relatively unimportant compared to their role in Co(IV).[6]

We also note that the electronic absorption spectra of the homoleptic V(IV) complex with π-donor ligands, namely, $V(NEt_2)_4$, has been recorded, both as a pure solid and in a $Ti(NEt_2)_4$ host.[43,74] These spectra gave shoulders at 17 300 cm^{-1} (17 065 cm^{-1} in the Ti(IV) host) and 13 000 cm^{-1} (13 120 cm^{-1} in Ti(IV)), which are quite close to those absorptions observed for **1**, but they were assigned oppositely, i.e., as $^2B_1 \rightarrow {}^2E$ and $^2B_1 \rightarrow {}^2B_2$, respectively. However, the

DOI: 10.1021/acs.inorgchem.5b02017
Inorg. Chem. 2015, 54, 10081−10095

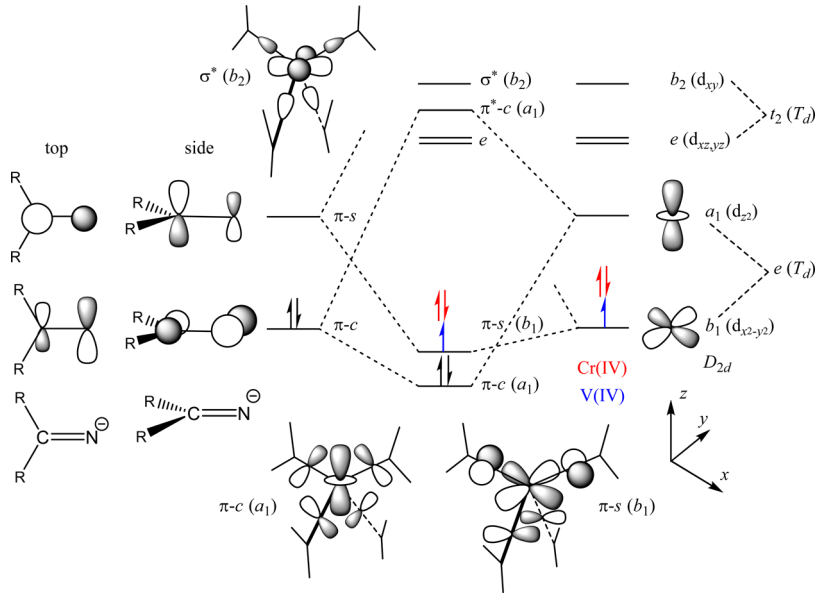

Figure 12. Qualitative MO diagram for V(IV) (d^1, blue electron) and Cr(IV) (d^2, red electrons) tetrakis(ketimide) complexes. On the far left is shown two views of the relevant ketimide π-MOs; on the far right is shown the most important metal 3d AOs, with their representations in T_d and D_{2d} symmetry. In the center is shown qualitatively the MOs resulting from interactions between the relevant ligand and metal orbitals, with representations in D_{2d} symmetry; quantitative results for V(IV) are shown in Figure 13. At the bottom is shown two of these resulting ketimide−metal MOs; for clarity, only the nitrogen p AO of the ketimide π-MO is shown in these diagrams. For completeness, at the top, the σ^* (b_2) MO is also shown, but interactions involving the unfilled d_{xz}, d_{yz} AOs are not shown.

authors were not adamant in this assignment as opposed to the reverse. These workers did not have a crystal structure; however, many years later, the structure of $V(NMe_2)_4$ was reported, and its geometry is much closer to tetrahedral symmetry (although still D_{2d}) than the geometry of the present group 5 ketimide complexes.[24] The application of modern computational methods, unavailable at the time of the EPR studies on tetra(amido) and (alkoxido) V(IV) complexes,[43,44] is therefore of interest but must be the subject of future investigations.

With this π-bonding model, the fit results are completely different. With three parameters ε_σ, $\varepsilon_{\pi-s}$, and $\varepsilon_{\pi-c}$, it is possible to fit the two transitions exactly. The difference from the above-mentioned σ-only analysis, however, is that while the transition at 12 800 cm^{-1} is still assigned to (allowed) $^2B_1 \rightarrow {}^2E$ and that at 16 000 cm^{-1} to (vibronically allowed) $^2B_1 \rightarrow {}^2B_2$, the forbidden $^2B_1 \rightarrow {}^2A_1$ transition is now calculated to occur at 14 800 cm^{-1}. This is fully possible, as it would lie under existing bands. The fit parameters are ε_σ = 3410 cm^{-1}, $\varepsilon_{\pi-c}$ = 4780 cm^{-1}, and $\varepsilon_{\pi-s}$ = −1840 cm^{-1}, so the ketimide ligands could be considered to be moderate σ-donors, strong π-donors, and strong π-acceptors. These ketimide bonding parameters can be put into the context of other ligands of interest, although such comparison data are relatively scarce. To our knowledge, these data are not available for the amide, $[NR_2]^-$, ligand, which is probably the most relevant comparison for this study. However, they are known for classical neutral N-donor ligands, such as NH_3, RNH_2 (as in ethylenediamine), and RR′NH (as in 1,4,8,11-tetraazacyclotetradecane (cyclam)) when ligated to first-row early transition metal ions such as Cr, mainly in the common 3+ oxidation state[72,73] but also in higher oxidation states such as Cr(V)[75] and Mn(V, VI).[76] Briefly, these σ-only donors exhibit $\varepsilon_\sigma \approx$ 7000 cm^{-1} (higher for the highly oxidized ions). Imine nitrogens donors come in many forms, but they can be good σ-donors with π-acceptor (or donor) ability, e.g., ε_σ = 6150 cm^{-1}, ε_π = −330 cm^{-1} for pyridine coordinated to Cr(III).[72] Pyrazole nitrogens, as found in the well-known "scorpionate" ligand (hydridotris(pyrazol-1-yl)borate, Tp^-), give ε_σ = 8350 cm^{-1}, $\varepsilon_{\pi-s}$ = 1300 cm^{-1} ($\varepsilon_{\pi-c}$ = 0) for $[Tp_2Cr]^+$,[77] with similar parameters estimated for Mn(III) in $[Tp_2Mn]^+$.[78] The extreme among N (or likely any other) donors is nitride, which exhibits ε_σ = 25 000 cm^{-1}, ε_π = 18 000 cm^{-1} for Cr(V) and Mn(V).[75,76] Phosphines bound to late transition metal ions, e.g., Ni(II), can be described as having $\varepsilon_\pi \approx -1500$ cm^{-1},[79] comparable to what is seen here for ketimide, and are good σ-donors ($\varepsilon_\sigma \approx$ 5000 cm^{-1}), but they have no simultaneous π-donor ability. Bonding parameter characterization of ketimides bound to a wider variety of metal ions is needed, but it is clear that, while being only moderate σ-donors, their combination of π-donor and π-acceptor abilities makes them unusual, if not unique, among N (or P) donor ligands.

We can also calculate EPR transitions using the LFT software DDN (see Supporting Information),[79] which also includes the electronic spin and orbital Zeeman interaction. Thus, application of an external magnetic field (B_0 = 350 mT, to correspond to X-band) and inclusion of spin−orbit coupling, ζ = 175 cm^{-1} (70% of the free-ion value, 250 cm^{-1})[80] yields $g_\parallel$ = 1.914 and $g_\perp$ = 1.974. These g values are more anisotropic and with lower g_{avg} than experiment, but the relation $g_\parallel < g_\perp < 2.00$ is reproduced. This is as expected from perturbation theory,[81] where the g values are described by

$$g_\parallel = g_e - \frac{8\zeta}{(E_{^2B_2} - E_{^2B_1})}, \qquad g_\perp = g_e - \frac{2\zeta}{(E_{^2E} - E_{^2B_1})} \tag{5}$$

where $(E_{^2E} - E_{^2B_1})$ = 12 800 cm^{-1} and $(E_{^2B_2} - E_{^2B_1})$ = 16 000 cm^{-1}, so that $g_\parallel$ = 1.915 and $g_\perp$ = 1.975, exactly the same values as the LFT exact calculation. The value for ζ could, of course,

DOI: 10.1021/acs.inorgchem.5b02017
Inorg. Chem. 2015, 54, 10081−10095

be reduced to improve the correspondence, e.g., $\zeta \approx 110$ cm^{-1} (44% of the free-ion value) matches the experimental $g_\perp$, although $\zeta \approx 50$ cm^{-1}, a meaninglessly low value for V(IV), is needed to match $g_\parallel$. As shown below, quantum calculations are much more successful at not overstating the g anisotropy in this complex.

We can apply the same model to the Nb(IV) complex, **2**. In this case, there may be rhombic splitting resolved in the visible region, with bands at 12 300, 14 300, 18 700 cm^{-1} and an additional band at 23 400 cm^{-1}. This is similar to a band at 21 400 cm^{-1} observed for $[V(C_6Cl_5)_4]$ by Alonso et al.,[41] but we do not attempt to assign it, as we doubt that these violet/blue absorption bands are d−d in character. We note that $[V(Mes)_4]$ exhibits several bands in this region (23 870, 21 480, 18 350 cm^{-1}), but all were assigned to CT transitions.[30] In any case, using the same fit procedure, the bands match exactly (the center of the first two bands is the fit result, 13 300 cm^{-1}).[82] The fit parameters for **2** are $\varepsilon_\sigma = 5210$ cm^{-1}, $\varepsilon_{\pi-c} = 4670$ cm^{-1}, and $\varepsilon_{\pi-s} = -1700$ cm^{-1}, so there is a stronger σ-bonding interaction with the larger Nb(IV) ion than with V(IV), with the π-bonding being roughly the same. This observation is consistent with what would be expected on going down a group in the d block.

In summary, with the ligand field analysis in hand, it is now apparent that the geometry differences observed for M(amide)$_4$ and M(ketimide)$_4$ are not due to differences in σ- or π-donor ability, which are probably similar between the two ligand types, but are instead due to the π-acceptor ability of the ketimide ligand, as the amide ligand is unable to act in this capacity.

Quantum Chemical Theory Analysis. Analogously to what was done previously for $[Co(N{=}C^tBu_2)_4]$,[6] we have used density functional theory (DFT) to probe the series of group 5 ketimides. In the interest of computational efficiency, complexes **1** and **2** were both truncated to M(N=CMe$_2$)$_4$. The program ORCA by Neese[83,84] was employed with the B3LYP functional and def2-TZVP basis set,[85,86] which are widely used for transition metal complexes.[87,88] Further details are given in Supporting Information, including representative input/output files, Tables S3 and S4, respectively, for $[V(N{=}CMe_2)_4]$ and $[Nb(N{=}CMe_2)_4]$. In the latter case, our computational methodology was still effective, with the only qualitatively relevant point being a greater delocalization onto the ketimide nitrogen orbitals. The key result for both the V and Nb ketimide complexes is that the appearance of the HOMO is clearly that which we have defined above as $d_{x^2-y^2}$, with a π^* interaction with the ketimide ligands, which is consistent with the ligand field analysis. This can be seen in Figure S25, which presents side-by-side the spin up (α) HOMOs for $[V(N{=}CMe_2)_4]$ (MO #73) and $[Nb(N{=}CMe_2)_4]$ (MO #82).

The frontier MOs for $[V(N{=}CMe_2)_4]$ with predominant 3d character (MOs #73−76 and 78) are shown in Figure 13, with their calculated energies and representations in D_{2d} symmetry. Immediately below the HOMO in energy are two degenerate π-bonding orbitals (MOs #71 and 72) that do have significant V 3d character. Their π-antibonding counterpart MOs with higher d character are shown in Figure 13. Overall, the MO diagram is very similar to that determined previously for the Co(IV) congener.[6] The chief difference between the two cases, besides the spin quartet d^5 configuration for Co(IV), is that the 3d-based MOs are overall higher in energy for V(IV), as expected from its being in group 5 as opposed to group 9, and the energy separation between the b_1 and e, a_1 MOs (i.e., the

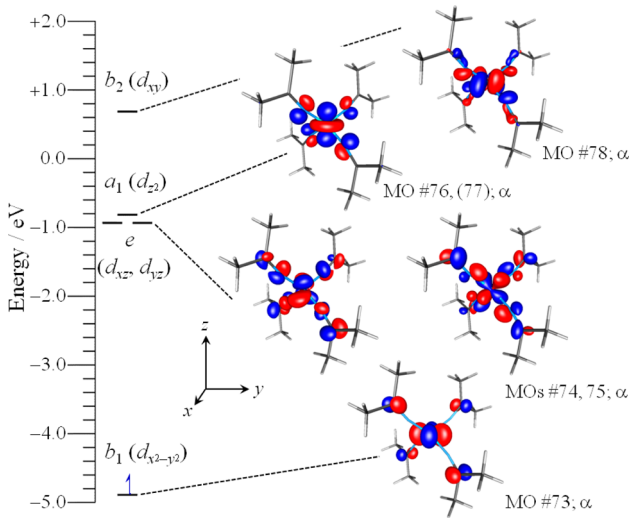

Figure 13. Frontier molecular orbitals for $[V(N{=}CMe_2)_4]$ with representations in D_{2d} symmetry. Isosurface value = 0.06.

HOMO−LUMO gap) is much larger as well (~4 eV for V(IV) versus ~2 eV for Co(IV)). Nevertheless, the extreme closeness in energy among the e, a_1 MOs (which are half-filled in $[Co(N{=}C^tBu_2)_4]$) is again found for the V(IV) complex. Although we have not specifically performed calculations for the Cr(IV) congener, it is clear from our MO diagram that this complex would have a filled b_1 HOMO with the triplet excited state(s) significantly higher in energy, in agreement with earlier work.[9]

The corresponding MO diagram for $[Nb(N{=}CMe_2)_4]$ is shown in Figure S26 (Supporting Information). The results are overall very similar to those for the V(IV) complex, with the Nb-based MOs being higher in energy. As a result, these are more in range with high-energy ligand-based MOs. Thus, there is a purely ketimide π^* MO (#86) lying in between two MOs each with Nb 4d$_{z^2}$ character, the latter of which (#87) appears to be a more classical 4d$_{z^2}$ orbital. Again, we have not performed calculations for the Mo(IV) congener, nor did Soriaga et al.,[9] but our results for $[Nb(N{=}CMe_2)_4]$ give a HOMO−LUMO gap of ~3 eV, so the singlet ground state for $[Mo(N{=}C^tBu_2)_4]$ should be greatly favored.

In addition to providing an MO picture of these group 5 ketimide complexes, ORCA software can calculate EPR parameters. In this case, this includes the **g** tensor, with its orientation, and the hyperfine coupling tensors both for these magnetically active metal ions and the ^{14}N atoms of the ketimide ligands. As seen in Table 3, which compares the experimental and calculated EPR parameters, the **g** tensor anisotropy in these complexes is relatively small, making computational reproduction of the experimental data challenging. What is gratifying, however, is that for both $[V(N{=}CMe_2)_4]$ and $[Nb(N{=}CMe_2)_4]$ an essentially axial **g** tensor is calculated with $g_\parallel < g_\perp < 2.00$. This is the result expected from simple LFT, as described above, but what is significant is that the calculated g values themselves are quite close to experiment, more so than from LFT, particularly for g_z ($g_\parallel$, g_{min}), which is the best determined among the various experimental parameters. For both V and Nb complexes, the **g** tensors derived from optimized geometries give slightly better agreement with experiment than those using the crystal structures. This may reflect the possibility that the solution structure of these complexes is less squashed than in the solid

DOI: 10.1021/acs.inorgchem.5b02017
Inorg. Chem. 2015, 54, 10081−10095

Table 3. Experimental and Calculated g Values and Metal (^{51}V, ^{93}Nb) and Ligand (^{14}N) Hyperfine Coupling Constants (in MHz) for Group 5 Ketimides[a]

complex		g_{iso} (fluid), g_{avg} (frozen)	g_z, g_x, g_y (frozen)[f]	a_{iso} (fluid), A_{avg} (frozen)[d]		A_z, A_x, A_y (frozen)[e]	A_{dip} (z, x, y)[f]
		isotope		^{51}V/^{93}Nb	^{14}N	^{51}V/^{93}Nb	^{51}V/ ^{93}Nb
[V(N=C^{t}Bu$_2$)$_4$], **1**	expt.	1.9885, 1.983	1.979, 1.985, 1.985	124, 125	10.5,	245, 65, 65	±120, ±60, ±60
[V(N=CMe$_2$)$_4$]	XRD[b]	1.9852	1.9824, 1.9866, 1.9864	−85.0	−12.8	−214.7, −19.8, −20.8	−129.7, +64.1, +65.6
	DFT[c]	1.9854	1.9756, 1.9903, 1.9903	−114.2	−11.5	−255.4, −43.3, −43.8	−141.2, +70.8, +70.4
[Nb(N=C^{t}Bu$_2$)$_4$], **2**	expt.	1.9840, 1.988	1.966, 1.999, 1.999	185, 150		300, 80, 80	±150, ±75, ±75
[Nb(N=CMe$_2$)$_4$]	XRD[b]	1.9803	1.9741, 1.9841, 1.9827	−190.3	−8.2	−315.0, −127.9, −128.0	−124.7, +62.4, +62.3
	DFT[c]	1.9803	1.9646, 1.9882, 1.9882	−203.8	−8.4	−340.1, −135.6, −135.6	−136.4, +68.2, +68.2

[a]No sign information on hyperfine coupling constants is available experimentally. [b]XRD = DFT calculation using X-ray diffraction (experimental) structure. [c]DFT = DFT calculation using DFT-optimized geometry. [d]The value presented for calculated a_{iso}(^{14}N) is an average of those for the four nitrogen ligands; however, the maximum variation among these calculated values is <0.05 MHz, less than experimental precision. [e]^{14}N hyperfine coupling was not resolved in frozen-solution EPR spectra; however, ENDOR spectroscopy recorded at a field corresponding to parallel (z) EPR transitions provided a value for A_z(^{14}N) ≈ 14 MHz (**1**) and 11 MHz (**2**). Quadrupole coupling was also estimated from these spectra: P_z(^{14}N) = 0.75 MHz (**1**) and 1.0 MHz (**2**). The maximum calculated quadrupole coupling was P_{max}(^{14}N) = 1.7 MHz, with a very rhombic tensor ($\eta = |P_{mid}| - |P_{min}|/|P_{max}|$ = 0.5 (**1**) and 0.7 (**2**)); if this were indeed the case, then analysis of a full field-dependent set of experimental ENDOR spectra would be problematic. [f]The calculated orientation of the **g** and metal nucleus **A** tensors is with the unique value (i.e., smallest g value, largest magnitude A value) along the molecular z axis, so $g_z \equiv g_{\|}$ and $A_z \equiv A_{\|}$, with the remaining, essentially equal components exactly in between the molecular x and y axes ($g_x \approx g_y \equiv g_{\perp}$ and $A_x \approx A_y \equiv A_{\perp}$), as defined in Figure 11 and in agreement with LFT.

state, but the agreement may be fortuitous. Regarding the hyperfine coupling, which is an even greater computational challenge, the results are also very satisfying. In this case, the experimental values for $A_{\perp}$(^{51}V, ^{93}Nb) are at best approximate, so the agreement in a_{iso} and A_{dip} may well be better than it appears. The calculated direction of the **g** and **A**(^{51}V, ^{93}Nb) tensors is as expected, with the unique (parallel) value aligned with the molecular approximate S_4 axis, in agreement with LFT. As seen in Table 3, the calculations reproduce the components of the axial **A**(^{51}V) tensor reasonably well, noting that the only well-determined experimental value is A_z ($A_{\|}$). Here, the results of the optimized geometry are clearly better than those from the experimental geometry, again supporting the idea that the solution structure is less squashed. However, the situation is less clear for **A**(^{93}Nb), where each geometry has strengths and weaknesses in terms of matching experiment. We also note that, since **2** did not give a single species upon freezing (and **7** was even more heterogeneous), the expectations for experimental and calculated correspondence for these complexes are inherently lower. Nevertheless, the calculated values for the ^{14}N hyperfine couplings are in reasonable agreement with the experimental values (see Table 3). Even the ^{14}N quadrupole couplings, of which only one component was estimated from ENDOR, are consistent between experiment and theory (Table 3). Interestingly, the calculated **P**(^{14}N) tensor was very rhombic [**P**(^{14}N) = [−0.40, −1.26, +1.66] MHz (**1**); [−0.25, −1.42, +1.67] MHz (**2**)], which may be a consequence of the complex σ-donation/π-donation/π-accepting nature of the metal−ketimide interaction, as described above, leading to a very nonspherical electron distribution around the nitrogen atoms. The quadrupole coupling tensors for ^{51}V and ^{93}Nb were also calculated and found to be small (e.g., P_{max}(^{51}V) = −0.17 MHz). For comparison, vanadyl complexes such as VO(salen) and VO(OEP) gave P_{max}(^{51}V) = −0.29 MHz.[58,59] One might expect a larger quadrupole in heteroleptic vanadyl complexes than in homoleptic **1**, but such generalizations are speculative given the paucity of such data. Overall, the calculated spin Hamiltonian parameters for **1** and **2** are fully consistent with experiment, especially given the deficiencies in experimental data and in computational modeling.

CONCLUSIONS

In summary, we have synthesized a series of homoleptic group 5 ketimide complexes, M(N=C^{t}Bu$_2$)$_4$ (M = V, Nb, Ta). With their syntheses, a nearly complete set of first-row M(N=C^{t}Bu$_2$)$_4$ complexes (M = Ti−Co), as well as two triads, the group 6 triad (which was reported by Hoffman and co-workers)[9] and now the group 5 triad, have been isolated and fully characterized. In the solid state, the group 5 ketimide complexes feature squashed tetrahedral (D_{2d}) geometries. Both EPR spectroscopic results and DFT calculations support a $d_{x^2-y^2}^1$ ($^2B_1$ in D_{2d}) ground state for this series of complexes. EPR spectroscopy also reveals that the M−L interaction in M(N=C^{t}Bu$_2$)$_4$ is far more covalent than the M−L interactions in the related tetra(aryl), tetra(amido), and tetra(alkoxo) vanadium(IV) complexes. A ligand field analysis of the vanadium and niobium congeners also supports the presence of a strongly covalent metal−ketimide interaction. Most importantly, however, this comprehensive investigation provides experimental verification that the ketimide ligand is a good σ-donor, strong π-donor, and strong π-acceptor, a combination that is not found in amine, imine, or phosphine ligands. The combination of strong π-donor and π-acceptor abilities places the ketimide ligand within a select group of organometallic ligands. For comparison, both the cyclopentadienyl anion and benzene can act as simultaneous π-donors and δ-acceptors, which is a similar bonding situation to that seen for ketimide.[89] Although it should be noted that Cp$^-$ is not considered to be a particularly good δ-acceptor ligand.[89,90] We suggest that the combined acceptor and donor abilities of the ketimide ligand should make it capable of stabilizing both high and low oxidation states at the same metal center, potentially permitting the development of unusual catalytic cycles.

ASSOCIATED CONTENT

Supporting Information

The Supporting Information is available free of charge on the ACS Publications website at DOI: 10.1021/acs.inorgchem.5b02017.

Crystallographic data (CIF).

DOI: 10.1021/acs.inorgchem.5b02017
Inorg. Chem. 2015, 54, 10081−10095

Experimental and computational details, spectral data, and additional figures and tables (PDF).

AUTHOR INFORMATION

Corresponding Authors

*(J.T.) E-mail: jtelser@roosevelt.edu.

*(T.W.H.) E-mail: hayton@chem.ucsb.edu.

Notes

The authors declare no competing financial interest.

ACKNOWLEDGMENTS

We thank the National Science Foundation (CHE 1361654) for financial support of this work. We thank Prof. Brian M. Hoffman, Northwestern University, for use of the X- and Q-band EPR spectrometers in his laboratory, which is supported by the NIH (GM 111097 to B.M.H.). We also thank Prof. T. David Harris and Kang Du, Northwestern University, for use of their glovebox and assistance with air-sensitive EPR sample preparation. We thank Dr. Andrew Ozarowski, National High Magnetic Field Laboratory, for providing the program CRYSTAL and assisting with its use. We thank Prof. Jesper Bendix, Copenhagen University, for providing the program Ligfield and helpful comments. Finally, we thank Dr. Guang Wu, University of California, Santa Barbara, for assistance in collecting X-ray crystallographic data and Anthony DeMartino for preliminary investigations in this area.

REFERENCES

(1) Kiplinger, J. L.; Morris, D. E.; Scott, B. L.; Burns, C. J. *Organometallics* **2002**, *21*, 3073−3075.

(2) Graves, C. R.; Vaughn, A. E.; Schelter, E. J.; Scott, B. L.; Thompson, J. D.; Morris, D. E.; Kiplinger, J. L. *Inorg. Chem.* **2008**, *47*, 11879−11891.

(3) Lewis, R. A.; Wu, G.; Hayton, T. W. *J. Am. Chem. Soc.* **2010**, *132*, 12814−12816.

(4) Lewis, R. A.; Wu, G.; Hayton, T. W. *Inorg. Chem.* **2011**, *50*, 4660−4668.

(5) Seaman, L. A.; Wu, G.; Edelstein, N.; Lukens, W. W.; Magnani, N.; Hayton, T. W. *J. Am. Chem. Soc.* **2012**, *134*, 4931−4940.

(6) Lewis, R. A.; George, S. P.; Chapovetsky, A.; Wu, G.; Figueroa, J. S.; Hayton, T. W. *Chem. Commun.* **2013**, *49*, 2888−2890.

(7) Lewis, R. A.; Smiles, D. E.; Darmon, J. M.; Stieber, S. C. E.; Wu, G.; Hayton, T. W. *Inorg. Chem.* **2013**, *52*, 8218−8227.

(8) Cotton, F. A.; Wilkinson, G.; Murillo, C. A.; Bochmann, M. *Advanced Inorganic Chemistry*, 6th ed.; John Wiley & Sons, Inc.: New York, 1999.

(9) Soriaga, R. A. D.; Nguyen, J. M.; Albright, T. A.; Hoffman, D. M. *J. Am. Chem. Soc.* **2010**, *132*, 18014−18016.

(10) Manzer, L. E. *Inorg. Chem.* **1977**, *16*, 525−528.

(11) Deutscher, R. L.; Kepert, D. L. *Inorg. Chem.* **1970**, *9*, 2305−2310.

(12) Schäfer, H.; Kahlenberg, F. *Z. Anorg. Allg. Chem.* **1960**, *305*, 178−189.

(13) Arteaga-Müller, R.; Tsurugi, H.; Saito, T.; Yanagawa, M.; Oda, S.; Mashima, K. *J. Am. Chem. Soc.* **2009**, *131*, 5370−5371.

(14) Marchetti, F.; Pampaloni, G.; Zacchini, S. *Dalton Trans.* **2008**, 7026−7035.

(15) Marchetti, F.; Pampaloni, G.; Zacchini, S. *Inorg. Chem.* **2007**, *47*, 365−372.

(16) Casanova, D.; Alemany, P.; Bofill, J. M.; Alvarez, S. *Chem. - Eur. J.* **2003**, *9*, 1281−1295.

(17) Mashima, K.; Tanaka, Y.; Nakamura, A. *Organometallics* **1995**, *14*, 5642−5651.

(18) Strauch, H. C.; Erker, G.; Fröhlich, R. *Organometallics* **1998**, *17*, 5746−5757.

(19) Martins, A. M.; Marques, M. M.; Ascenso, J. R.; Dias, A. R.; Duarte, M. T.; Fernandes, A. C.; Fernandes, S.; Ferreira, M. J.; Matos, I.; Conceição Oliveira, M.; Rodrigues, S. S.; Wilson, C. *J. Organomet. Chem.* **2005**, *690*, 874−884.

(20) Heinselman, K. S.; Miskowski, V. M.; Geib, S. J.; Wang, L. C.; Hopkins, M. D. *Inorg. Chem.* **1997**, *36*, 5530−5538.

(21) Marchetti, F.; Pampaloni, G.; Zacchini, S. *Dalton Trans.* **2007**, 4343−4351.

(22) Marchetti, F.; Pampaloni, G.; Zacchini, S. *Eur. J. Inorg. Chem.* **2008**, *2008*, 453−462.

(23) Yang, L.; Powell, D. R.; Houser, R. P. *Dalton Trans.* **2007**, 955−964.

(24) Dubberley, S. R.; Tyrrell, B. R.; Mountford, P. *Acta Crystallogr., Sect. C: Cryst. Struct. Commun.* **2001**, *57*, 902−904.

(25) Yamada, J.; Fujiki, M.; Nomura, K. *Organometallics* **2005**, *24*, 2248−2250.

(26) Zhang, W.; Nomura, K. *Inorg. Chem.* **2008**, *47*, 6482−6492.

(27) Yamada, J.; Fujiki, M.; Nomura, K. *Organometallics* **2007**, *26*, 2579−2588.

(28) Onishi, Y.; Katao, S.; Fujiki, M.; Nomura, K. *Organometallics* **2008**, *27*, 2590−2596.

(29) Zhang, W.; Yamada, J.; Nomura, K. *Organometallics* **2008**, *27*, 5353−5360.

(30) Głowiak, T.; Grobelny, R.; Jeżowska-Trzeblatowska, B.; Kreisel, G.; Seidel, W.; Uhlig, E. *J. Organomet. Chem.* **1978**, *155*, 39−46.

(31) Bott, S. G.; Hoffman, D. M.; Rangarajan, S. P. *Inorg. Chem.* **1995**, *34*, 4305−4310.

(32) Perera, T. H.; Lord, R. L.; Heeg, M. J.; Schlegel, H. B.; Winter, C. H. *Organometallics* **2012**, *31*, 5971−5974.

(33) Mashima, K.; Matsuo, Y.; Tani, K. *Organometallics* **1999**, *18*, 1471−1481.

(34) Krishnamurthy, R.; Schaap, W. B. *J. Chem. Educ.* **1969**, *46*, 799−810.

(35) Suh, S.; Hoffman, D. M. *Inorg. Chem.* **1996**, *35*, 5015−5018.

(36) Lehn, J.-S. M.; van der Heide, P.; Wang, Y.; Suh, S.; Hoffman, D. M. *J. Mater. Chem.* **2004**, *14*, 3239−3245.

(37) Wilson, R.; Kivelson, D. *J. Chem. Phys.* **1966**, *44*, 154−168.

(38) Labauze, G.; Samuel, E.; Livage, J. *Inorg. Chem.* **1980**, *19*, 1384−1386.

(39) Muller, E. G.; Petersen, J. L.; Dahl, L. F. *J. Organomet. Chem.* **1976**, *111*, 91−112.

(40) Muller, E. G.; Watkins, S. F.; Dahl, L. F. *J. Organomet. Chem.* **1976**, *111*, 73−89.

(41) Alonso, P. J.; Forniés, J.; García-Monforte, M. A.; Martín, A.; Menjón, B. *Chem. - Eur. J.* **2005**, *11*, 4713−4724.

(42) Kirmse, R.; Stach, J.; Kreisel, G. *J. Organomet. Chem.* **1981**, *210*, 73−82.

(43) Holloway, C. E.; Mabbs, F. E.; Smail, W. R. *J. Chem. Soc. A* **1968**, 2980−2984.

(44) Kokoszka, G. F.; Allen, H. C., Jr.; Gordon, G. *Inorg. Chem.* **1966**, *5*, 91−93.

(45) Froncisz, W.; Hyde, J. S. *J. Chem. Phys.* **1980**, *73*, 3123−3131.

(46) Alonso, P. J.; Ara, I.; Arauzo, A. B.; García-Monforte, M. A.; Menjón, B.; Rillo, C. *Angew. Chem., Int. Ed.* **2010**, *49*, 6143−6146.

(47) Bigmore, H. R.; Zuideveld, M. A.; Kowalczyk, R. M.; Cowley, A. R.; Kranenburg, M.; McInnes, E. J. L.; Mountford, P. *Inorg. Chem.* **2006**, *45*, 6411−6423.

(48) Green, J. C.; Green, M. L. H.; Kaltsoyannis, N.; Mountford, P.; Scott, P.; Simpson, S. J. *Organometallics* **1992**, *11*, 3353−3361.

(49) Noh, W.; Girolami, G. S. *Inorg. Chem.* **2008**, *47*, 535−542.

(50) Munhá, R. F.; Zarkesh, R. A.; Heyduk, A. F. *Inorg. Chem.* **2013**, *52*, 11244−11255.

(51) Nguyen, A. I.; Blackmore, K. J.; Carter, S. M.; Zarkesh, R. A.; Heyduk, A. F. *J. Am. Chem. Soc.* **2009**, *131*, 3307−3316.

(52) Petersen, J. L.; Griffith, L. *Inorg. Chem.* **1980**, *19*, 1852−1858.

(53) Mailer, C.; Taylor, C. P. S. *Biochim. Biophys. Acta, Protein Struct.* **1973**, *322*, 195−203.

(54) Baute, D.; Goldfarb, D. *J. Phys. Chem. A* **2005**, *109*, 7865−7871.

DOI: 10.1021/acs.inorgchem.5b02017
Inorg. Chem. 2015, 54, 10081−10095

(55) Mustafi, D.; Galtseva, E. V.; Krzystek, J.; Brunel, L.-C.; Makinen, M. W. *J. Phys. Chem. A* **1999**, *103*, 11279−11286.
(56) Kirste, B.; Van Willigen, H. *J. Phys. Chem.* **1982**, *86*, 2743−2749.
(57) Mulks, C. F.; Kirste, B.; Van Willigen, H. *J. Am. Chem. Soc.* **1982**, *104*, 5906−5911.
(58) Aznar, C. P.; Deligiannakis, Y.; Tolis, E. J.; Kabanos, T.; Brynda, M.; Britt, R. D. *J. Phys. Chem. A* **2004**, *108*, 4310−4321.
(59) Grant, C. V.; Ball, J. A.; Hamstra, B. J.; Pecoraro, V. L.; Britt, R. D. *J. Phys. Chem. B* **1998**, *102*, 8145−8150.
(60) Fallis, I. A.; Murphy, D. M.; Willock, D. J.; Tucker, R. J.; Farley, R. D.; Jenkins, R.; Strevens, R. R. *J. Am. Chem. Soc.* **2004**, *126*, 15660−15661.
(61) Mustafi, D.; Makinen, M. W. *Inorg. Chem.* **2005**, *44*, 5580−5590.
(62) McGarvey, B. R. *J. Phys. Chem.* **1967**, *71*, 51−66.
(63) These values are calculated using the reported frozen-solution average values for a_{iso}, g_{iso}; use of the fluid-solution values gives $|P|$ = 318.8 MHz and $|\kappa|$ = 0.510.
(64) For **7**, $|P|$ = 152 MHz and $|\kappa|$ = 1.6. This value of $|\kappa| > 1$ is not physically reasonable (i.e., a larger coupling than in the free ion). The lack of definitive EPR low-temperature data for **7** makes this analysis inapplicable compared to the V and Nb ketimides.
(65) Even if C_{2v} symmetry is used, this transition, which becomes $^2A_2 \rightarrow {}^2A_1$, is still forbidden.
(66) In T_d symmetry, this transition directly gives Δ_{tet}; in C_{2v} symmetry, this would simply split into $^2A_2 \rightarrow {}^2B_1$ (d_{xz}, y allowed) and $^2A_2 \rightarrow {}^2B_2$ (d_{yz}, x allowed).
(67) Clark, R. J. H.; Machin, D. J. *J. Chem. Soc.* **1963**, 4430−4433.
(68) Note that if the ground state were $^2A_1$, then this transition would be allowed with z polarization. Again, even if C_{2v} symmetry is used, this transition, which becomes $^2A_2 \rightarrow {}^2A_1$, is still forbidden.
(69) Considering only the MN_4 core, the nine normal vibrational modes in D_{2d} are: a_1 (×2, IR forbidden), b_1 (IR forbidden), b_2 (×2, IR allowed), and e (×2, IR allowed). Note that lower case is used for vibrations to distinguish from electronic transitions. Vibronic coupling with the e modes would make this electronic transition allowed: $a_1 \times {}^2B_1 \times (E) \times {}^2B_2 \times (e) = A_1 + ...$
(70) Riley, M. J.; Hitchman, M. A.; Mohammed, A. W. *J. Chem. Phys.* **1987**, *87*, 3766−3778.
(71) Alonso et al., in their study of in situ generated $[V(C_6Cl_5)_4]$, reported bands at 14 950 and 16 680 cm^{-1} (there appears to be no resolution between these bands; the higher one could charitably be called a shoulder). See ref 41.
(72) Figgis, B. N.; Hitchman, M. A. *Ligand Field Theory and Its Applications*; Wiley-VCH: New York, 2000.
(73) Miessler, G. L.; Fischer, P. J.; Tarr, D. A. *Inorganic Chemistry*; Pearson: Upper Saddle River, NJ, 2014.
(74) The UV−vis spectrum of the related homoleptic alkoxido complex, $V(O^tBu)_4$, consists of a single broad band at 13 500 cm^{-1}, simply assigned to $^2E \rightarrow {}^2T_2$ in T_d symmetry. See ref 44.
(75) Meyer, K.; Bendix, J.; Bill, E.; Weyhermüller, T.; Wieghardt, K. *Inorg. Chem.* **1998**, *37*, 5180−5188.
(76) Meyer, K.; Bendix, J.; Metzler-Nolte, N.; Weyhermüller, T.; Wieghardt, K. *J. Am. Chem. Soc.* **1998**, *120*, 7260−7270.
(77) Fujihara, T.; Schönherr, T.; Kaizaki, S. *Inorg. Chim. Acta* **1996**, *249*, 135−141.
(78) Forshaw, A. P.; Smith, J. M.; Ozarowski, A.; Krzystek, J.; Smirnov, D.; Zvyagin, S. A.; Harris, T. D.; Karunadasa, H. I.; Zadrozny, J. M.; Schnegg, A.; Holldack, K.; Jackson, T. A.; Alamiri, A.; Barnes, D. M.; Telser, J. *Inorg. Chem.* **2013**, *52*, 144−159.
(79) Desrochers, P. J.; Telser, J.; Zvyagin, S. A.; Ozarowski, A.; Krzystek, J.; Vicic, D. A. *Inorg. Chem.* **2006**, *45*, 8930−8941.
(80) Bendix, J.; Brorson, M.; Schäffer, C. E. *Inorg. Chem.* **1993**, *32*, 2838−2849.
(81) McGarvey, B. R. In *Transition Metal Chemistry*; Carlin, R. L., Ed.; Marcel Dekker: New York, 1966; pp 89−201.
(82) It is possible to match all of the bands exactly by dividing the ligands into pairs, but this allows for six fit parameters and is thus overparametrized.
(83) Neese, F. *ORCA—an ab initio, Density Functional and Semiempirical Program Package*, 3.0.3; Max Planck Institut für Chemische Energiekonversion: Mülheim an der Ruhr, Germany, 2014. https://orcaforum.cec.mpg.de/.
(84) Neese, F. *Wiley Interdisciplinary Reviews: Computational Molecular Science* **2012**, *2*, 73−78.
(85) Schäfer, A.; Horn, H.; Ahlrichs, R. *J. Chem. Phys.* **1992**, *97*, 2571−2577.
(86) Weigend, F.; Ahlrichs, R. *Phys. Chem. Chem. Phys.* **2005**, *7*, 3297−3305.
(87) Roemelt, M.; Neese, F. *J. Phys. Chem. A* **2013**, *117*, 3069−3083.
(88) Maganas, D.; Sottini, S.; Kyritsis, P.; Groenen, E. J. J.; Neese, F. *Inorg. Chem.* **2011**, *50*, 8741−8754.
(89) Rayón, V. M.; Frenking, G. *Organometallics* **2003**, *22*, 3304−3308.
(90) Crabtree, R. H. *The Organometallic Chemistry of the Transition Metals*, 3rd ed.; John Wiley & Sons: New York, 2001.

DOI: 10.1021/acs.inorgchem.5b02017
Inorg. Chem. 2015, 54, 10081−10095